SOLID PARTICLE EROSION OF CERAMICS

by

R.G WELLMAN

A thesis submitted to the Faculty of Engineering, University of Cape Town, in fulfilment of the Degree of Master of Applied Science

July 1993

Department of Materials Engineering

Acknowledgements

I would like to thank all those who assisted me in producing this thesis.

Prof. C Allen, my supervisor, for his support and guidance.

Nick Dreze, Glen Newins and Dave Dean, for their technical assistance.

Bernard Greeves and James Petersen for the photographic work.

Staff and fellow students for their support and assistance with the computers.

Eskom for their financial support of this project.

CONTENTS

SYNOPSIS

One of the major areas of wear in the generation of power from coal occurs in the pipes transporting the pulverised fuel from the coal mills to the burners. This erosion of the pipes is vastly accelerated at the pipe bends, hence the choice of lining material is extremely important.

This project addresses the problem through the systematic erosion testing, at different angles of impact, of fifteen erosion resistant materials to determine the feasibility of their use as lining materials. Two were tungsten carbide cobalt cermets whilst the others were all ceramics, most of which were various grades of alumina plus basalt and glass. Other factors examined in this work are the effects of erodent type, particle size and velocity on erosion rates.

It has been shown that the relative hardnesses of the target and erodent does not provide a clear prediction of erosion resistance. However, microtoughness, measured using the indentation method, and modulus of rupture have been found to give a good indication of erosion resistance for the materials tested.

Threshold velocity and angle effects have also been observed in the ceramics and have been ascribed to a change in the erosion mechanism. It has been found that at high angles of impact, 90° & 60°, material removal is via the formation of lateral fracture and the formation and removal of chips from the surface. At the lower angles of impact, 45° & 30°, damage appears to be predominantly plastic in nature with damage accumulation necessary prior to the formation of lateral cracks and loss of material.

NOMENCLATURE

PF	Pulverised fuel
MD	Moh-9 manufactured 50% alumina ceramic
MZF	Moh-9 manufactured zirconia toughened alumina
M97F	Moh-9 manufactured 97% fine grained alumina
M97	Moh-9 manufactured 97% alumina
M94	Moh-9 manufactured 94% alumina
M94F	Moh-9 manufactured 94% fine grained alumina
M99	Moh-9 manufactured 99% alumina
90% Jap	Japanese manufactured 90% alumina
90% Germ	German manufactured 90% alumina
MT	Multotek manufactured 90% alumina
10%Co-WC	10% cobalt tungsten carbide composite
6%Co-WC	6% cobalt tungsten carbide composite
87% US	US manufactured 87% alumina
H_t	Target hardness
H_p	Particle hardness
R_c	Radius of Curvature
D	Pipe diameter
H_v	Vickers hardness
Pc	Critical load for crack initiation in ceramics

CHAPTER 1

INTRODUCTION

In many situations wear is caused by hard particles carried in either an air or liquid stream striking surfaces of materials. This type of wear is termed erosion, qualified as solid particle erosion to distinguish it from the damage caused by the impact of liquid droplets. Erodent particles can be as large as 1 mm in diameter and can reach velocities of 550 m/s. When these values of velocities and particle size are exceeded the damage is referred to as foreign object damage.(1)

Coal fired power stations experience such erosive wear on the inner walls of pipelines used in the pneumatic transportation of the pulverised fuel (PF) to the burners, which is exacerbated at bends where the erosion rate can be as much as 50 times greater than in the straight sections (1). Typically the size of the PF varies from 1 to 300 microns and is in concentrations in the region of 0.6 kg/m^3. The velocity of the PF in the pipes varies from 24 to 30 m/s.

South African coal is of low calorific value and contains large quantities by volume of alumino-silicates, which are extremely abrasive particles. The ash constitutes from 20 to 50% by weight of the PF, the alumino-silicate species together with quartz accounts for 60 to 90% by weight of the ash. As alumino-silicates and quartz are abrasive materials the erosion propensity of coal will depend largely on the content of these minerals (2).

The current trend to combat the erosive wear in these pulverized fuel pipelines is to use a variety of erosion

resistant ceramic pipe liners in the form of tiles which, despite their generally low fracture toughness, have a superior erosion resistance to metals. A number of different ceramic and other pipeliners are currently available with varying mechanical properties, grain size and composition. However little is known about the relative performance of such materials despite their extensive use in the power industry

Whilst the mechanism of particle erosion of brittle materials is well understood and documented the relationship of the erosion rate of ceramics to their mechanical and constitutional properties is less well modelled.

AIM

The aim of the work was to facilitate the selection of materials for use as pipeliners to minimise erosive wear during the pneumatic transportation of pulverised fuel.

OBJECTIVE

The specific objectives of the work were to:

a) Evaluate a range of proprietary ceramic and other materials for use in the pulverised fuel pipelines.

b) Ascertain the mechanisms of erosion.

c) Relate the wear performance to material properties and constitution.

d) Make specific recommendations on cost effective materials selection to minimise erosive wear.

CHAPTER 2

LITERATURE REVIEW

2.1 EROSION MECHANISMS

Two main types of response to solid particle impact have been observed, one being characteristic of ductile materials, mostly metals, the other being characteristic of brittle materials such as glasses and ceramics. The difference is evident from an examination of erosion rate with the angle of impact. Brittle materials generally exhibit a maximum material loss at 90° impact while the more ductile materials experience maximum material loss at approximately 30° (3). These two different responses are illustrated in figure 2.1 and discussed in sections 2.2 and 2.3.

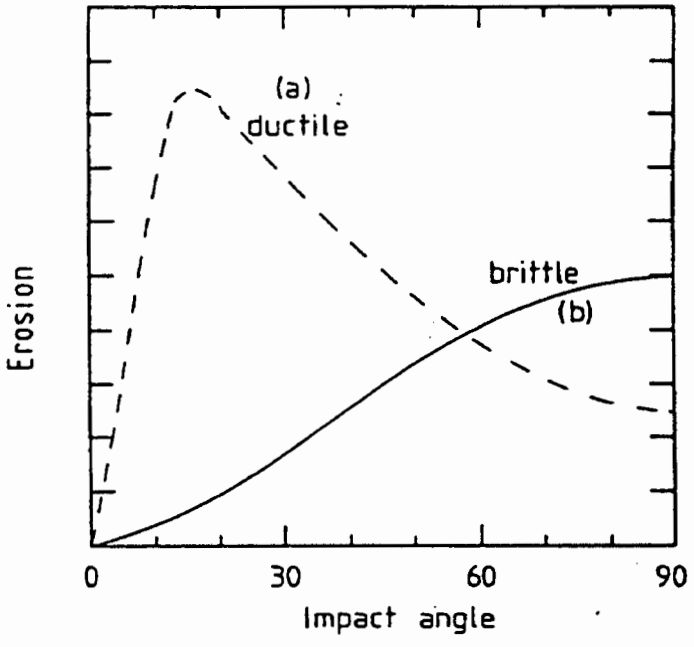

Fig 2.1: Effect of angle on material loss (3).

2.2 IMPACT DAMAGE IN DUCTILE MATERIALS

The erosion of soft, tough materials is predominantly ductile and material loss can occur in two different ways: cutting wear due to impact at low angles (4) shown in figure 2.2, and extrusion at high angles shown in figure 2.3. Fragmentation of the impacting particles can occur at normal or near normal impact angles giving rise to secondary erosion (5). These two modes do not exclude each other, erosion of ductile materials is essentially a combination of the two processes.

2.2a CUTTING WEAR

Ductile erosion reaches a maximum at a particular angle of impact due to cutting wear. The impacting particle removes material by chip formation, essentially scraping material off the surface of the solid (4). This is illustrated in figure 2.2.

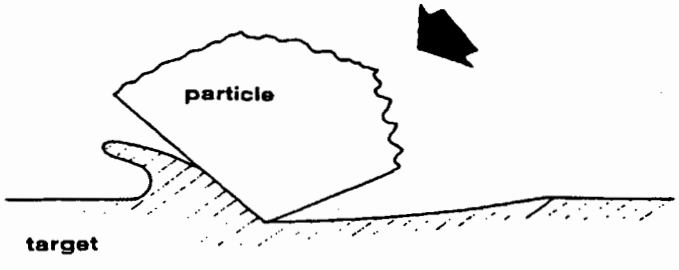

Fig 2.2: Material loss through cutting wear (4).

2.2b EXTRUSION AND FRAGMENTATION

When the eroding particle strikes the surface of a ductile material at or near 90° the material is extruded to the edge

of the damage zone to form lips that will then be vulnerable to subsequent impacts (5, 6). These subsequent impacts will cause further extrusion and work hardening until fracture occurs and the material is completely removed from the surface. A secondary stage can also occur, if the impacting particle is brittle and fragments during impact. Secondary erosion can occur when the fragmented pieces scour the surface, this is illustrated in fig 2.3.

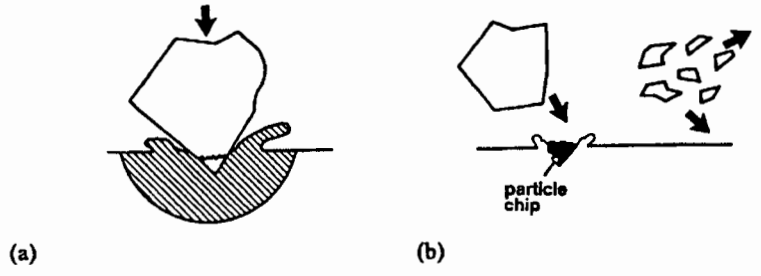

Fig 2.3: Extrusion and fragmentation (5).

2.3 IMPACT DAMAGE IN BRITTLE MATERIALS

Material loss in solid particle erosion of brittle materials occurs through the formation and interaction of a subsurface microcrack network. In order for these cracks to develop the surface stresses must reach a critical value to initiate microcracking. When these cracks propagate and intersect with the surface, material is lost (4, 7-11). Hence for a brittle material to have a good erosion resistance it must have a high fracture toughness and a high resistance to crack initiation.

The modes of deformation and fracture depend on the particle velocity, shape and mechanical properties relative to those of the target material (4, 12-14). Blunt particles travelling at low velocities set up elastic Hertzian stress fields in the target which initiates cone cracking. Sharp particles travelling at high velocities produce inelastic deformation

zones and initiate median and lateral cracking (15).

2.3a MEDIAN / LATERAL CRACKING

When eroding with relatively hard or incompressible particles the target is plastically deformed and two primary types of fracture can occur. Median cracks which propagate downward from the contact zone and lateral cracks which develop below the contact zone and propagate parallel to the surface eventually curving up towards the surface (7). These cracks exhibit some similarities to the median and lateral cracks observed during quasi-static indentation (10).

Lawn and Swain (16) have described the loading sequence for a sharp indentor, this is illustrated in figure 2.4.

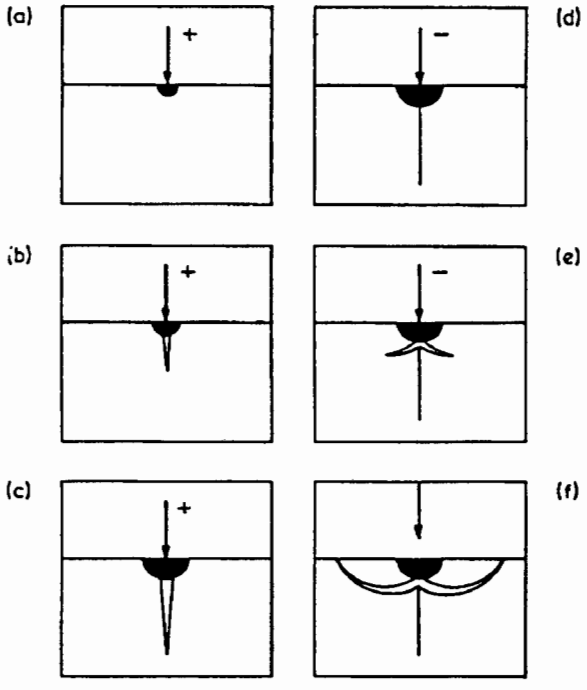

Fig 2.4 The development of radial/lateral cracks (16).

A zone of irreversible deformation is induced around the sharp indentor which increases with increasing load (a). At some critical load a crack suddenly initiates under the contact point where the stress concentration is greatest (b). This crack is called the median crack and increasing the load will cause further extension of the median vent (c). On initial unloading the median vent begins to close but does not heal (d). Relaxation of deformed material within the contact zone just prior to removal of the indentor superimposes intense residual tensile stresses upon the applied field. This causes the initiation of sideways-extending cracks called lateral cracks (e). On complete unloading (f) the lateral crack continues to grow and can intersect with the surface causing chipping (10, 16-18).

2.3b HERTZIAN CRACKING

When a blunt elastic particle impacts on a brittle material, which remains elastic until fracture occurs, Hertzian cone cracks will develop. Material removal will depend on the propagation of the fracture into the material and its interaction with other fractures. The development of Hertzian cone cracks is illustrated in figure 2.5.

On initial loading a compressive field is set up directly beneath the indentor, with a tensile stress outside the expanding contact circle (a). Upon attaining a critical Griffith configuration a surface flaw runs around the area of contact to form a ring crack, which will extend downwards out of the surface skin region (b). As loading increases tensile stresses accumulate until the ring crack spontaneously develops into a full cone crack. On unloading, the cone crack tries to close and heal in order to recover some of the stored elastic energy but is prevented from doing so by the mechanical obstruction of debris (c). If the unloading is

rapid enough the base of the cone may turn up in a hat brim fashion (4 & 8).

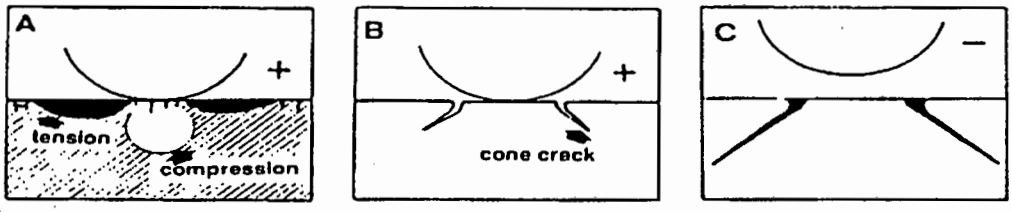

Fig 2.5: The development of cone cracks (8).

2.4 EROSION OF DUAL PHASE MATERIALS

The erosion behaviour of dual-phase materials (DPMs), such as tungsten carbide cobalt cermets, containing ductile and brittle phases is often different from that expected based on the erosion response of the individual constituents. The erosion of DPMs can be fully understood only if the size of the impact damage zone relative to the microstructural size is known (19-21). In this regard, two situations exist.

Case a

The impact damage zone is appreciably larger than the size of the second phase particles or the surrounding matrix, illustrated in fig 2.6. The erosion behaviour in this case has similarities with that of ductile materials, with a maximum erosion rate occurring at an oblique angle (i.e. between 20° to 60°). The angle at which maximum erosion occurs increases with the increasing volume fraction of the brittle phase. The predominant erosion mechanism in this case will be ductile. No simple correlation between the erosion rate of the mixture and that of the individual phases exists, i.e. the erosion rate cannot be expressed in terms of any rule

of mixtures.

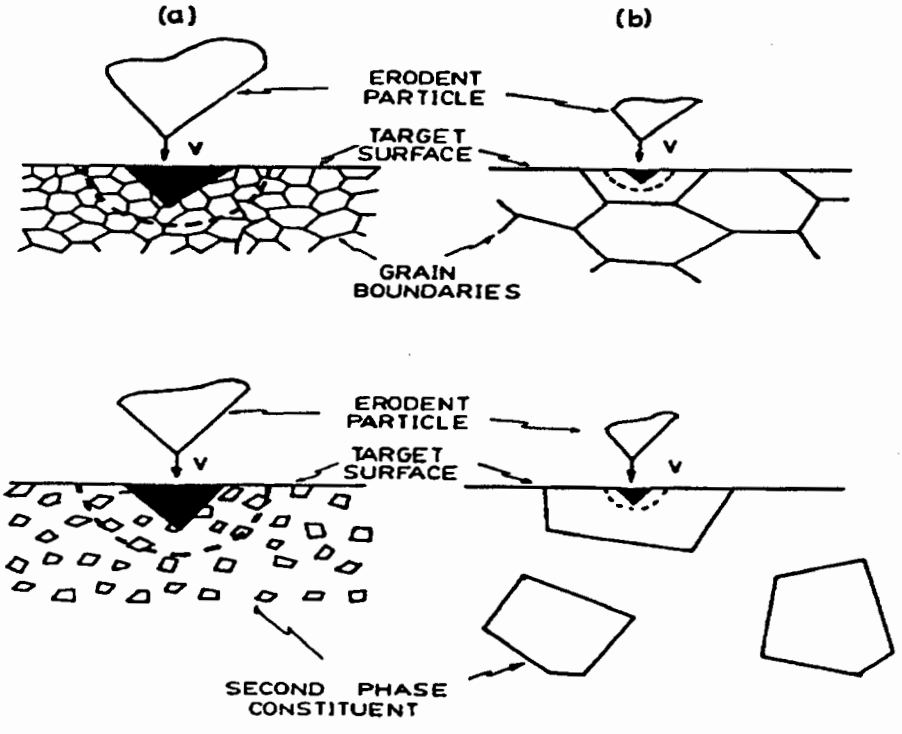

Fig 2.6: The erosion of dual-phase materials (21).

Case b

The size of the impact damage zone is smaller than the microstructural feature size. For such a situation, the ductile and brittle constituents are sampled separately by the erodent particle and the erosion rate of the alloy can often be expressed in terms of the erosion rates of the individual phases through a rule of mixtures. For example, the erosion behaviour of a composite consisting of alumina rods (500μm diameter) in a stainless steel matrix could be modelled by a linear rule of mixtures (21). Further, studies on the erosion of Al-Si alloys found that the erosion rate followed an inverse rule of mixtures when the impact damage was small enough to sample the Al-Si eutectic and the primary Si phases separately. It is worth noting however that enhanced erosion

rates due to edge spalling of brittle particles for DPMs containing large brittle particles in a ductile matrix has been observed, leading to a departure from predictions based on a rule of mixtures.

2.5 VARIABLES AFFECTING EROSION

The wear of materials is systems related and thus changes to the system variables is critical in determining the material loss. The velocity, impact angle and concentration of the impacting particles as well as the temperature of the gas stream will all have different effects on the rate of material removal (12, 15, 22-24).

The other important variables are the mechanical properties of the erodent particles with respect to those of the target material. The hardness, density and fracture toughness (K_{IC}) of both erodent and target affects the erosion rate. The shape and size of the erodent and the microstructure of the target influences the erosion mechanism which also determines the erosion rate.

2.6 PARTICLE VARIABLES

2.6a DENSITY AND SIZE:

The erosion rate of brittle materials is, in theory, expected to increase monotonically as particle size increases and erosion studies have supported this assumption (25). A threshold particle size, below which no erosion occurs, may exist (26), although conclusive evidence verifying this existence has, as yet, not been reported.

In ductile materials, the erosion rate is significantly reduced when impacting particles are below a certain threshold size of about 20 microns. This size varies for different systems. It is generally believed that the larger size particles are more erosive than smaller sized particles (22, 23, 27).

In the erosion of both ductile and brittle materials the particle size distribution is very important. A mixture of different particle sizes will produce a greater erosion rate than the sum of the individual components (22). When particles are accelerated under the same pressure, the smaller particles cause higher erosion rates due to their considerably higher velocities and due to the dependence of erosion rate on velocity. This can lead to an underestimate of the erosion rates in simulation tests if the incorrect particle size distribution is used.

2.6b SHAPE, HARDNESS AND FRACTURE TOUGHNESS

In both ductile and brittle materials a greater erosion rate is generally associated with more angular particles (23). It has been shown that shape and hardness of the particle determines the depth of the impact in the target material and hence affects the erosion rate of the material (28). Elastic contact of blunt particles with the target leads to the development of Hertzian cone cracks which tend to develop during erosion. Sharp particles on the other hand tend to set up higher stress fields due to the smaller contact area, which leads to the development of radial cracks which are associated with a greater material loss.

Surprisingly, Wada (12) found that increasing the ratio of target hardness to the hardness of the impacting particle (H_t/H_p) results in a dramatic increase in the erosion rates.

This was determined for ratios in the ranges of unity and using particles of about 1000 microns in size. Vaughan (29) on the other hand found that when the erodent particles are slightly harder than the target materials, the erosion rates are relatively high. Furthermore, there is a sudden decrease in erosion rate correlating with a hardness ratio of about unity after which there is a slight decrease in erosion rates with increasing target hardness. Vaughan used 120 grit silica, alumina and silicon carbide particles to erode various grades of alumina and ultra hard materials at 40 m/s.

The fracture toughness of a particle will determine whether the particle will fragment on impact, hence absorbing some of the impact energy. This reduces the energy that is transferred to the target and will consequently reduce the erosion rate (30).

2.7 TARGET VARIABLES

2.7a FRACTURE TOUGHNESS AND HARDNESS

Most brittle erosion models involve the initiation and propagation of cracks in the target, hence the fracture toughness of the material (the ability to resist crack growth) will influence the erosion rate. Sharp particles are more prone to develop half-penny cracks with local plastic damage and, on unloading, some lateral spalling (31). In general, under given conditions, the minimizing of lateral spalling through effective energy absorption (i.e. high K_{IC}) will improve the erosion resistance. Fracture toughness has often been related inversely to erosion rates in equations predicting the volume loss of an eroded surface (1, 14, 15, 31).

The target hardness will determine the (H_t/Hp) ratio which as mentioned earlier is important to erosion rates. The hardness of the target will also determine the degree of plastic deformation which affects the size of the contact area and hence the driving force for lateral crack formation.

2.7b MICROSTRUCTURE

Since the erosive damage in brittle materials is often of a similar size to the grain size, the microstructure of a material will affect the erosion rate (30). Porosity for example affects the erosion rate of a material by inhibiting crack propagation by blunting crack tips (15). Equally, lateral cracks which form on impact can either be contained within the grain or pass through many grains. In the latter case crack propagation will be inhibited by the grain boundaries. This effectively reduces the size of the damage zone and reduces erosion rates. Breder et al (32) also observed this dependence on grain size.

Non-cubic polycrystalline ceramics show a strong grain size dependence of strength (17). This dependence is due to thermal expansion and the subsequent internal stresses.

It was found that in MgO, cracking along the grain boundaries occurred in the vicinity of the impact site leaving loosely connected grains which are then easily removed from the surface on subsequent impacts. This mechanism is vastly different from other mechanisms and leads to high material losses (15).

2.8 SYSTEM VARIABLES

2.8a CONCENTRATION

The effect of particle concentration on erosion is primarily due to the increased probability of collision between the incident and rebounding particles as particle concentration increases.

At high particle concentration the erosion rate of a material decreases with an increase in the particle concentration due to this effect. Uuemous and Klies found this to be true for metals, alloys and ceramics but not for rubber and some plastics (1, 22, 33).

The explanation for this decrease in the erosion rates is due to the impacting particles and debris rebounding and interacting with incoming particles hence reducing the number of impacts on the target. With rubber, compared to brittle materials, the duration of impact and depth of penetration is greater and the energy of the rebounding particle is lower hence there is less protection by rebounding particles.

2.8b VELOCITY AND ANGLE OF IMPACT

Particle velocity is an important variable in particle erosion since it strongly influences the impact energies. Lateral cracking is more prevalent at high velocities giving rise to greater erosion rates (31). By reducing the angle of impact of the particles with respect to the target the amount of energy that will be transferred to the target will be reduced and hence the erosion rate will also reduce. Wiederhorn et al (28, 34) found that the strength degradation suffered by glass

surfaces in sharp particle impact diminishes as the impact occurs more obliquely, and that the damage sites were indeed smaller at 15° impact than at 90° impact. This is only true when dealing with erosion of brittle materials. In ductile erosion there is a maximum erosion rate at about 30°-60°.

The vector of a particle can be resolved into two components, one perpendicular to the target and one parallel to the target. The energy transferred to the target is dependent on the size of the perpendicular vector component and as the angle of impact decreases, so does the size of the perpendicular vector component and the energy of impact.

2.8c AERODYNAMIC EFFECTS

Due to the aerodynamic effects on the particles in the air stream the erodent particles never strike the target at the apparent angle except at the stagnation point as illustrated below in figure 2.7 (35-37).

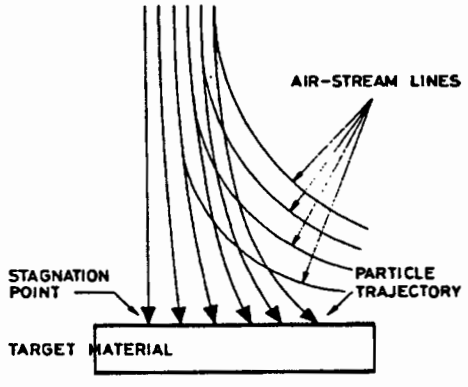

Fig 2.7: Aerodynamic effects on the angle of impact (36).

This implies that the angle of impact is always lower than the apparent angle. This effect applies to all angles of impact and not just 90°.

Laitone (36) has defined two cases dealing with two phase flow:

1) In the limiting case where all the particles are sufficiently small that the airstream density approaches that of the fluid, the particles don't impact the surface but follow the fluid streamlines around the target.

2) As the particles momentum increases, the trajectory of the particles deviate from the fluid streamlines. In the case where the particles have a high momentum the particles travel in straight line trajectories determined by the initial conditions.

In practice most common flows fall between the two cases and the particle deflection can be expected to occur. The amount of deflection will depend on the particle density, size, shape and velocity and on the fluid density and velocity.

Tangential drag forces will not increase the particle impact velocity compared to those arising in the absence of drag. It is incorrect to assume that the particle velocity on impact is the same as that measured away from the target surface (36).

2.9 THE EFFECTS OF PIPE DIAMETER AND RADIUS OF CURVATURE ON THE WEAR RATES OF PIPES

Pneumatic systems transporting gas-borne solids do not usually suffer from particle-impaction erosion in straight flow sections other than from some small particles impacting at low, glancing angles, which cause negligible wear. However, at pipe bends, elbows and dividing sections, excessive wear will occur. The particle impact sites at the pipe bend will be different for particles of different sizes and densities

due to the effects of the drag force exerted on the particles by the gas flow (38). Figure 2.8 indicates this phenomena.

Smaller particles will be carried farther down stream from the pipe bend and impact the pipe wall at low angles in segment A. The impact of larger particles will take place in segment B at a higher angle.

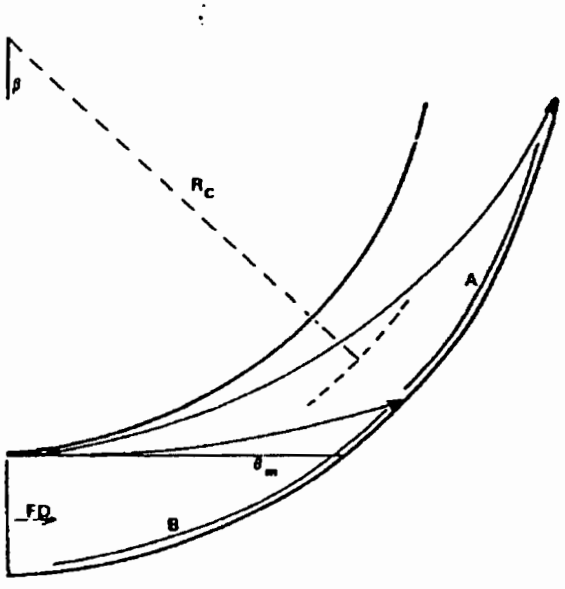

Fig 2.8: Particle trajectories in a pipe bend (38).

In the transportation of both small, low density and large, high density particles the bend acts as a material separator. However, when dealing with PF, the bend does not act as a material separator since the particle stream consists of small, high density (mineral matter) and large, low density (coal) particles. In this case the majority of wear takes place in segment C at relatively high angles, as illustrated in figure 2.9.

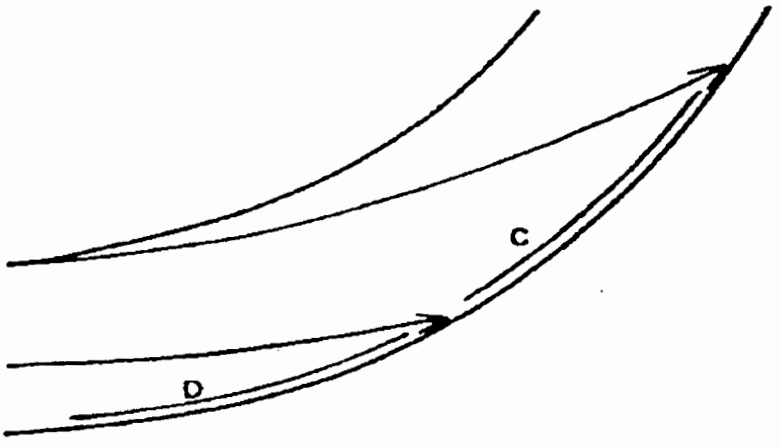

Fig 2.9: Coal particle trajectories in pipe bends (38).

In the pneumatic transportation of pulverized fuel (PF) the ratio of pipe diameter to the radius of curvature will determine the maximum angle of impact of the particles which is an important factor in determining the wear rate of a pipe. The maximum angle ($\tilde{O}_m$) is calculated according to the following equations (38).

$$\text{Cos } \tilde{O}_m = (R_C - 0.5)/(R_C + 0.5)$$

$$\tilde{O}_m = \tan^{-1}[(2R_C/D)^{0.5} (R_C/D)^{-1}]$$

where R_C is the radius of curvature and D is the pipe diameter.

The South African power industry (Eskom) has R_C/D ratios ranging from 1.6 to 5.3 although it has now been specified that ratios of less than 3.5 may not be used in new stations. Table 2.1 contains a range of R_C/D ratios and the corresponding maximum angles of impact as calculated using the above equations.

R_C/D	$\tilde{O}_m$ (°)
1.6	58.4
1.8	55.6
2.0	53.1
2.2	51.0
2.4	49.1
2.6	47.3
2.8	45.8
3.0	44.4
3.5	41.4
4.0	38.9
4.5	36.8
5.0	35.1

Table 2.1: R_C/D ratios and corresponding maximum angle of impact.

It can be seen that the larger the ratio the smaller the maximum angle of impact. Since ceramics are more erosion resistant at lower angles, design must incorporate as large a ratio as possible.

2.10 THE EROSIVE PROPERTIES OF COAL

The abrasive properties of pulverized coal depends mainly on the quantity of hard, sharp-edged quartz and pyrites particles present in the fuel, which are the hardest of the mineral matter present in coal.

The mineral matter in coal is present as a sediment of fine

clay particles and as much larger pieces of rock. Table 2.2 shows the hardness of the constituents of coal(2).

	Mohs Hardness	Vickers Hardness
Coal		10-70
SILICATES:		
Kaolin	2-2.5	30-40
Illite	2-2.5	20-35
Muscovite	2-2.5	40-80
Kyanite	4-7	500-2150
Topaz	8	1500-1700
CARBONATES:		
Calcite	3	130-170
Magnesite	4	370-520
Siderite	4	370-430
Quartz	7	1200-1300
Pyrites	6-7	1100-1300
Alumina	9	2150

Table 2.2: Vickers hardness of the constituents of coal (2)

In South African coal the silicates account for 55-60% percent of the ash while the aluminas account for 24-30% and iron in the form of pyrites accounts for 0.5-7% of the ash. Table 2.3 is a full list of the volume fraction of the different constituents of South African coal ash.

Mineral	% In ash
Silicon	55-60
Aluminium	24-29
Iron	0.4-7.8
Calcium	4.3-5.9
Titanium	1.2-1.5
Sulphur	0.1-0.4
Magnesium	1.4-1.7

Table 2.3: The constituents of South African coal ash (39).

Coal and micas (illites and muscovites) have hardnesses below 70 Vickers and can therefore be considered to be soft materials which do not cause any significant erosion of either the milling plant or the pulverized fuel conveying pipes.

Quartz and pyrites which are present in the coal have a high Vickers hardness number (greater than 1000) and account for a high proportion of the erosive wear in the pipes. Power stations using coal with a high quartz and pyrites content have significantly higher erosion rates than stations using low quartz and pyrites coal. The other hard minerals orthoclase, kyanite, topaz and alumina are usually present only in trace quantities and are therefore unlikely to cause significant erosion.

CHAPTER 3

MATERIALS

The materials for this project were chosen on the basis of availability and suitability for use as erosion resistant linings. Of the 15 materials that were tested there were 11 aluminas of various grades, two tungsten carbide cobalt specimens, one glass sample and one basalt sample.

Basalt is currently utilised extensively in the power industry for the lining of the pipes used in the transportation of the pulverised fuel from the mills to the burners. Although basalt performs well in the straight sections, at pipebends its life is drastically reduced. For this reason it was proposed that a more wear resistant material be found for use at the pipe bends. Hence various grades of aluminas were chosen for erosion testing as possible substitutes for the basalt.

Although more expensive, the aluminas may be a cost effective solution due to a decrease in the down time needed for replacing worn tiles. Two grades of tungsten carbide-cobalt cermets were included in the erosion tests, since they are known as erosion resistant materials but they may prove to be prohibitively expensive. A glass tile was also included in the test matrix as a cheaper alternative to the other materials. Although the glass tiles would need to be replaced more often the cost of the tile could off set the cost of the added down time needed for tile replacement. The properties of the materials are listed in table 3.1.

MATERIAL	FRACTURE TOUGHNESS $MN/m^{3/2}$	HARDNESS DETERMINED Hv (30Kgf)	HARDNESS GIVEN* Hv	PERCENT Alumina
BASALT	0.901	876	900	15-17%
ALUMINAS				
MD	1.135	1037	1050	50%
MZF	4.259	1524	1500	**
M97F	3.465	1865	1900	97%
M97	2.897	1648	1900	97%
M94	2.973	1764	1800	94%
M94F	3.348	1789	1800	94%
M99	3.893	2006	2000	99%
90%Jap	3.696	1814	1780	90%
MT	1.701	1346	9-Moh	90%
87%US	3.076	1268	1650	87%
90%GERM	2.612	1072	1750	90%
Glass	0.712	1150	**	-
6%Co-WC	10.4	1583	1500	-
10%Co-WC	14.0	1235	1250	-

*Table 3.1: The mechanical properties of the materials that were tested: * manufactures values, ** Values not supplied.*

3.1 TARGET MATERIALS

3.1a ALUMINA

Alumina has a distorted hexagonal close packed (hcp) crystal structure. It has a 37% covalent nature resulting from the

small, highly charged Al^{3+} ions which causes a distortion of the close packed structure which also results in large thermal and elastic anisotropy.

In general the strength of alumina is largely dependent on composition (% alumina), porosity, grain size and finishing conditions. There is a large amount of scatter in strength, generally about 20%. This is due to the fact that fractures originate from inhomogeneous regions such as grain boundaries, pores and impurity inclusions.

The aluminas that were chosen range in alumina content from 50% to 99% and consequently they have different mechanical properties. Both locally produced aluminas and foreign products were tested.

A zirconia toughened alumina was also tested. Zirconia (zirconium oxide) is added to the alumina in order to improve its mechanical properties. Zirconia exists in two forms tetragonal or monoclinic. There is a 3-5% volume increase on transformation between tetragonal and monoclinic forms. When a crack extends under an applied load through the alumina matrix, the large tensile stresses will interact with the metastable tetragonal precipitates of zirconia. If this stress is sufficiently large it initiates a phase transformation. The volume increase associated with the transformation results in a nett compressive stress field and increases the effective energy to fracture and the toughness of the alumina.

The following three scanning electron microscope (SEM) micrographs, figures 3.1a-c, illustrate the microstructure of the alumina samples. Figures 3.1a and 3.1b are of M94F and M94 respectively and show the difference between the two microstructures. It should be noticed that there is a wide grain size distribution. This wide grain size distribution

was noticed in all the Moh-9 manufactured ceramics except for the M99 which had a narrow grain size distribution, the grain size varied by less than 20% for M99.

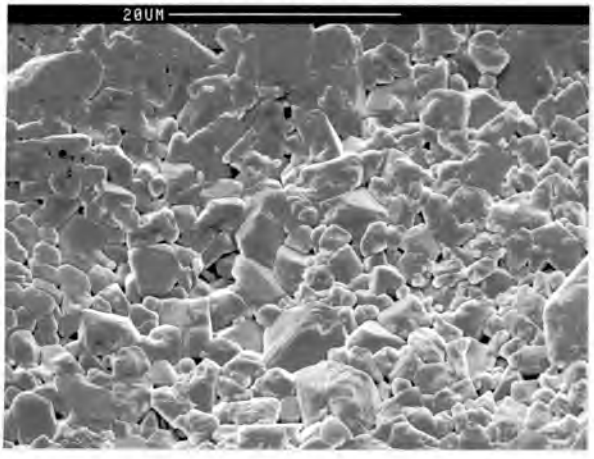

Fig 3.1a

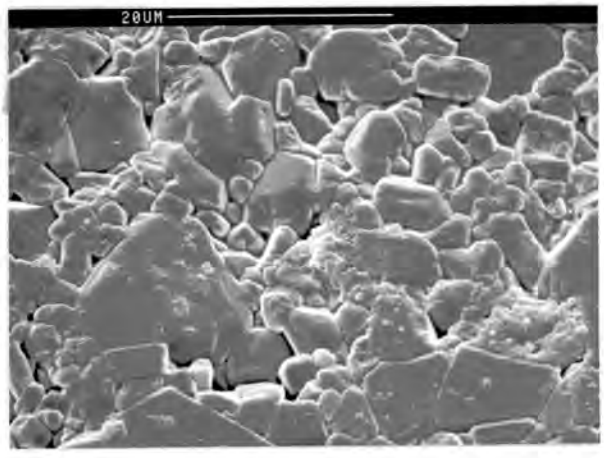

Fig 3.1b

Fig 3.1a & b: SEM micrographs of the microstructure of M97F (a) and M97 (b). Note the rounded grains and wide grain size distribution.

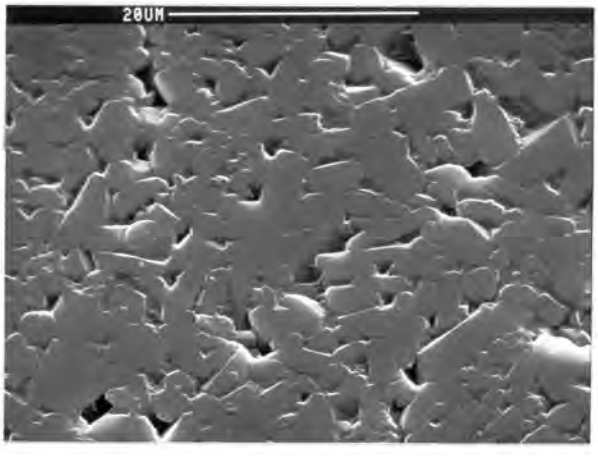

Fig 3.1c: The microstructure of the MT 90% alumina. Note the cuboid grains and the grain size distribution is considerably smaller than that of the 97% aluminas.

The imported ceramics had narrow grain size distributions with the exception of the US 87% alumina which had a fairly wide grain size distribution. The majority of the aluminas exhibited rounded grains but both the MT 90% alumina and the

US 87% alumina had an elongated cuboid type grain structure. A SEM micrograph, figure 3.1c, illustrates this cuboid type microstructure.

3.1b BASALT

Basalt is the name applied to the solid rock and to the magma, which upon eruption becomes lava. It is a dark-coloured fine grained rock with labradorite feldspar as the chief constituent of the groundmass. The groundmass of some basalts contains small amounts of interstitial glass and in rare instances is wholly glassy (40). This material consists mainly of SiO_2 (50-57%) with Al_2O_3 (15-17%), Fe_2O_3, FeO and CaO. Figure 3.2 is a SEM micrograph of the microstructure of basalt.

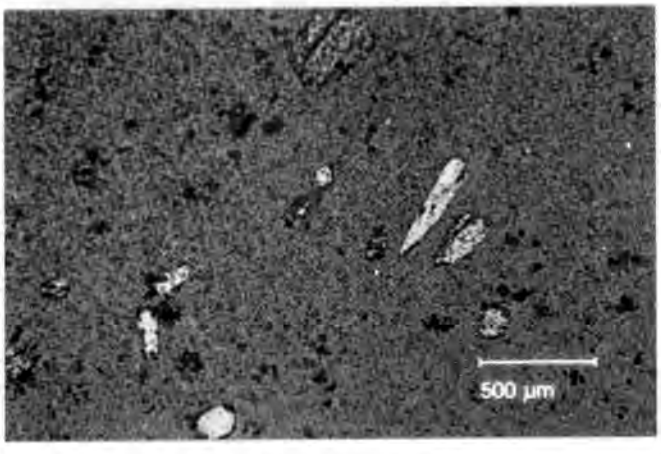

Fig 3.2: SEM micrograph of the microstructure of basalt. The white phase is alumina in the fine grained groundmass the dark phase.

They are generally porous materials and are relatively soft when compared to the aluminas. Inherent flaws in all basalts gives rise to low mechanical properties and toughness. Although the properties of basalt are poor when compared to those of alumina its low cost often makes it a far more viable option than alumina as a lining material.

3.1c TUNGSTEN CARBIDE COBALT CERMETS

Two tungsten carbide cobalt specimens with different cobalt percentages, namely 6% and 10%, and a grain size of 2-3 microns were also tested. Due to tungsten carbide's extremely hard and brittle nature it is usually used with a metal binder phase in the form of a cermet. This combination provides a wear resistant material with a relatively high hardness and a fracture toughness far greater than the aluminas. The microstructure of the 6% cobalt cermet is illustrated in figure 3.3 below.

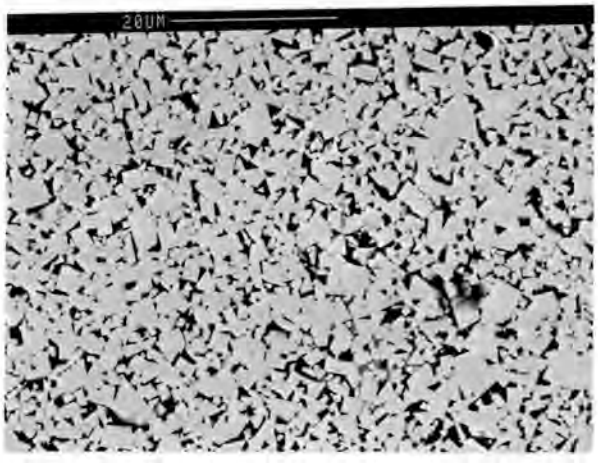

Fig 3.3: SEM micrograph of the microstructure of the 6% cobalt cermet, light phase WC, dark phase Co.

The appropriate combination of hardness and strength for a particular application may be controlled by varying the WC grain size and the percentage cobalt present (41). The hardness of WC-Co cermets decreases with an increase in cobalt content.

3.1d GLASS

A South African manufacturer has started producing cheap glass

tiles which might be a viable option as a lining material. The utilization of such a material might result in more frequent shut downs for relining, of the pulverized fuel lines, but this could be offset by the cost of the glass tiles relative to that of the aluminas. When compared to the aluminas, the glass has a very low fracture toughness and hardness but the ease and cost of the manufacturing techniques could compensate for their disadvantages.

3.2 ERODENTS

Three different erodents SiO_2, Al_2O_3 and SiC were used during the course of the experiments as shown in table 3.2. T.M Karlsen (42) found that the most suitable substitute for pulverised fuel for use in accelerated erosion tests was 115 micron SiO_2 particles. This decision was based on the consideration of both particle and damage parameters. For this reason the 120 grit size (106-125μm) SiO_2 was used to test all the materials at four different angles. The other two erodents were chosen in order to ascertain the effects of erodent properties, which are listed in table 3.2. These erodents Al_2O_3 and SiC were only used on the 94% aluminas in order to determine the effects of different types of erodents.

Erodent	Hardness (Hv)	Shape	Density (S.G)	Size range (microns)
Al_2O_3	1800	Sharp	3.99	106-125
SiC	2500	Angular	3.21	106-125
SiO_2	1100	Rounded	2.63	125-150
SiO_2	1100	Rounded	2.63	106-125
SiO_2	1100	Rounded	2.63	<75

Table 3.2: Erodent properties (29).

3.2a SILICON OXIDE

The three different sizes of SiO_2 that were used were 150-125μm, 125-106μm and less than 106μm. Figures 3.4a-c are SEM micrographs of the three different sizes. The SiO_2 grit was obtained from a local manufacturer and was sieved to obtain the desired size ranges. The SiO_2 is a fairly rounded and highly friable erodent.

a: SiO_2 size 150-125 microns.

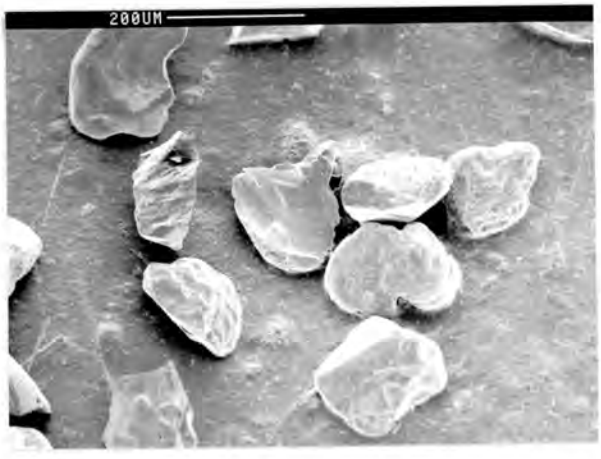

b: SiO_2 size 125-106 microns.

c: SiO_2 size < 106 microns.

Fig 3.4a-c: SEM micrographs of the 3 different SiO_2 particle sizes used. Note the rounded nature of the grains in each case.

3.2b ALUMINA

The Al_2O_3 particles were obtained locally. The particles have sharp corners and edges and are not as friable as the SiO_2 particles. 120 grit alumina was used in the erosion tests. Figure 3.5 is a SEM micrograph of the alumina that was used.

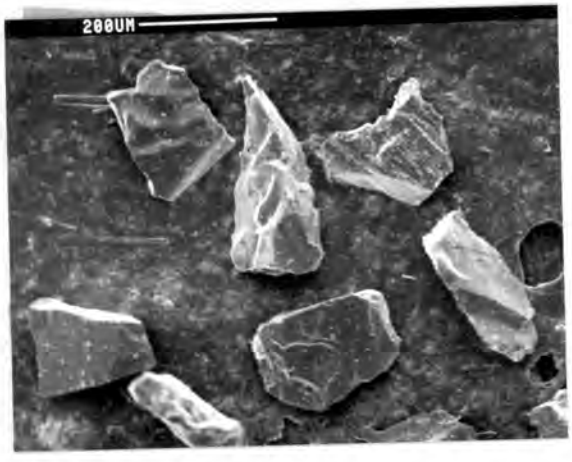

Fig 3.5: SEM micrograph of the alumina erodent. Note the angularity in these particles.

3.2c SILICON CARBIDE

The SiC was also supplied from Research Instrumentation and a grit size of 120 was used, illustrated in figure 3.6. The particles are extremely sharp and angular and were the least friable of the erodents used.

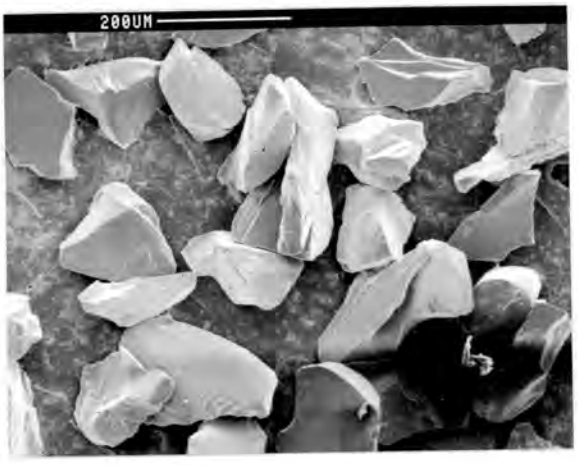

Fig 3.6: SEM micrograph of the SiC erodent. Again note the angularity in the particles.

CHAPTER 4

EXPERIMENTAL PROCEDURES

4.1 SAMPLE PREPARATION

All the samples were cut from commercial square tiles to the desired size (12mm by 12mm) on a diamond saw and then ground on a 600 grit wheel. They were then polished to a 1 micron finish using diamond paste. The samples were all mounted in a cold setting resin in order to facilitate the polishing. In order to remove the surface damaged zone caused by grinding, the samples were polished on cloth for 4.5 hours. A six micron diamond paste was used for the first 2.5 hours and then a 2.5 micron paste for a further 2 hours. The surface roughness was then measured using a profilometer to check that a 1 micron finish had been obtained. Six readings were taken for each sample, the variation was found never to be greater than 8%. After polishing, the samples were removed from the resin in order to run the tests.

4.2 APPARATUS

The erosion rig used for this work is represented schematically in figure 4.1. The compressed air is fed into the tube at point (a) at the desired pressure. The erodent is fed into the system at a fixed feed rate via a nozzle at point (b) and joins the air stream via a venturi at point (c). The feed rate is determined by the diameter of the nozzle and is easily measured by determining the time for a set amount of erodent to pass through the nozzle. The particles accelerate down the 3m long, 10mm diameter stainless steel tube, until they reach terminal velocity which is determined by the shape,

size and density of the particle and the air pressure which is controlled at point (d).

The angle of the target with respect to the air stream, the exposed surface of the target and the distance of the target from the tube can be varied (e). The air and particles are then separated via a cyclone system to ensure that dust free air emerges into the laboratory (g) and the used particles are collected. The used particles are collected at the points F1 and F2.

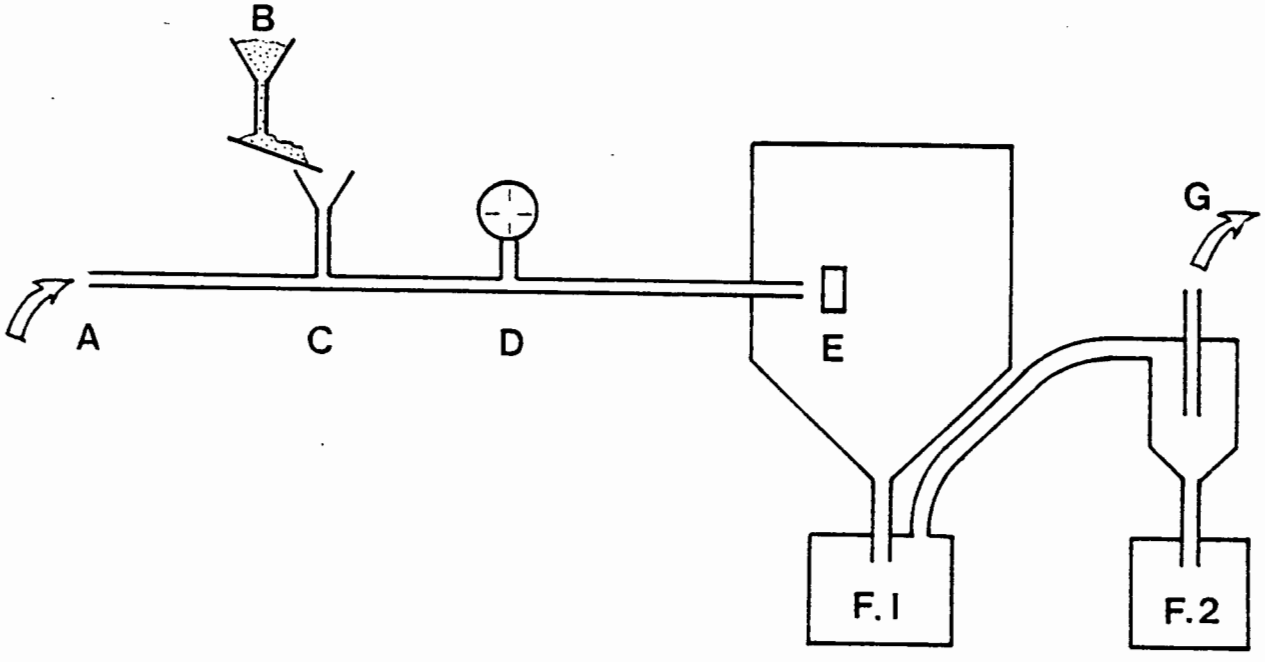

Fig 4.1: Schematic representation of the erosion rig used.

4.3 DETERMINATION OF EROSION RATES

The samples were all eroded under standard experimental conditions, summarised in table 4.1, for each angle. The

steady state erosion rates were calculated from the cumulative mass losses of eight consecutive erosion tests using linear regression and reported as mass loss per gram of erodent. In order to ascertain the reproducibility of the experiments duplicate tests were performed on some of the samples the results are shown in appendix 4. Between each test, the samples were washed in alcohol in an ultrasonic bath for 5 seconds. They were then dried thoroughly and weighed on an analytical balance, which was accurate to 0.01mg.

During all the tests that were conducted the samples were placed at a distance of 3 cm from the outlet of the tube and an area of 53 mm^2 was exposed to the particle stream.

Erodents	Al_2O_3 120 grit SiC 120 grit SiO_2 100, 120 & 140 grit
Impact angle	30°, 45°, 60° & 90°
Velocity	30 m/s, 40 m/s & 50 m/s
Working distance	3 cm
Operating temperature	Room temperature
Particle feed rate	0.446 g/s

Table 4.1: Operating conditions.

All 15 materials were eroded at 40 m/s at the four different angles of impact with SiO_2 (120 grit) particles. Two samples namely M94 and M94F were also eroded at 40 m/s and 60° using 120 grit SiC and Al_2O_3 and 100 and 140 grit SiO_2. Similar samples were then also eroded using 120 grit SiO_2 at 60° and 30 m/s and 50 m/s respectively.

The velocity of 40m/s was chosen as the test velocity as this is the upper limit experienced in the pulverised fuel lines. The erodent feed density was far lower than the density in the pulverised fuel lines and was chosen for optimum erosion rates.

4.4 THE EFFECTS OF PULVERIZED FUEL ON EROSION AS OPPOSED TO QUARTZ

It was originally intended to carry out erosion tests with pulverised fuel on the 94% alumina samples in order to obtain a direct comparison between pulverised fuel and SiO_2. Due to the tendency of the coal particles to agglomerate in the apparatus blocking the feed pipes and the Venturi it was not possible to use pulverised fuel as an erodent, without substantial modifications to the existing wear rig. Furthermore the erosiveness of different pulverized fuels varies enormously (26).

However, previous work has been conducted comparing the erosion rates of various pulverised fuels and other erodents (26). It was found that 115 μm diameter quartz was the most suitable substitute for the Pulverised fuel for use in accelerated erosion testing. This finding was based on the similarities of both particle parameters and the damage parameters. It was noted that the Quartz was between 21 and 100 times more erosive than the pulverised fuels at a velocity of 35m/s and an impact angle of 90°.

4.5 STANDARDIZATION OF EROSION RATES

During erosion testing a cover was placed over the target in order to ensure that a standard area (53 mm^2) was exposed to the erodent stream. Consequently not all the particles in the emerging gas stream were striking the test material. This is

illustrated in figure 4.2. This results in a lower apparent erosion rate for the material compared to a similar material tested without a cover when all the particles strike the surface. As all the materials were tested in an identical manner this factor can be ignored when comparing the results of ceramics tested at the same angle. However, the results of different impact angles can not be compared without standardization. This is due to the fact that when the angle of impact is decreased, the amount of the erodent striking the surface decreases, since the equivalent area perpendicular to the gas-particle stream decreases, this is illustrated in figure 4.2.

This problem was overcome using a simple correction factor which was experimentally determined. In order to standardize the erosion rates, two glass samples were tested at each angle, one exposing only the 53 mm^2 and the other large enough to allow all the impacting particles to strike the surface. The percentage difference in mass loss between the two was then used as the correction factor for that angle.

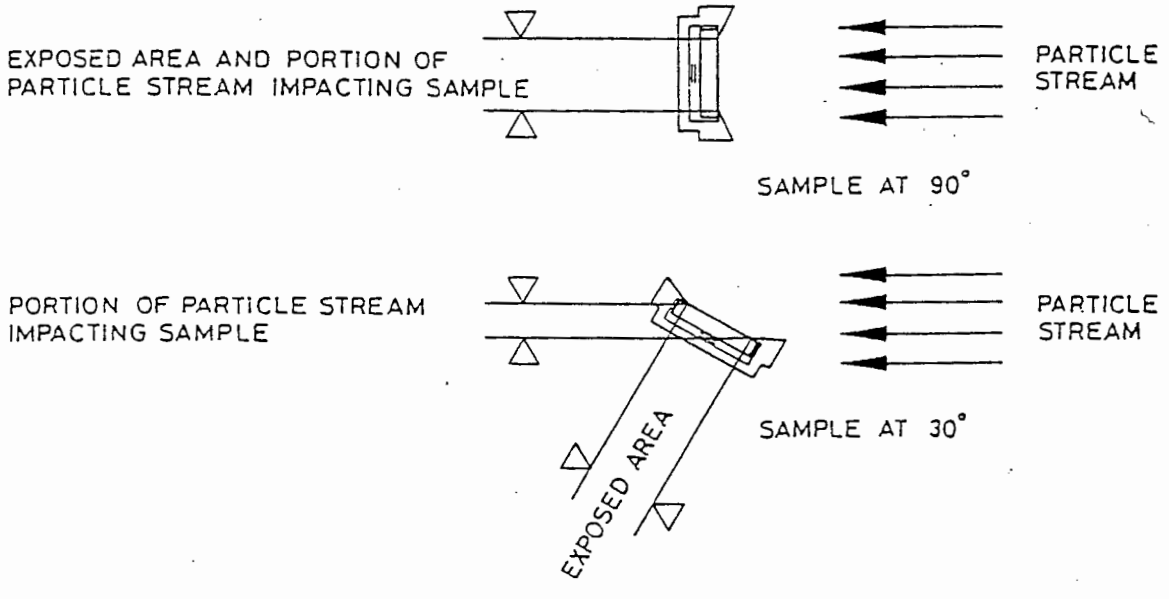

Fig 4.2: The effect of impingement angle on amount of erodent striking the target surface.

4.6 FRACTURE TOUGHNESS AND HARDNESS DETERMINATION

Erosion of ceramics is largely determined by the initiation and propagation of cracks caused by the impacting particles. This implies that the fracture toughness of ceramics is an important property when considering erosion resistance of such ceramics.

There are various methods available for the determination of the fracture toughness of ceramics (7 & 43-47). The method that has been used in this study is the indentation method, which yields values for the Mode 1 critical stress intensity factor K_{IC}. This method was chosen as it requires small samples and was easy to expedite.

The method involves the measurement of the crack length formed at the corners of a diamond shape indent at loads greater than the critical load for crack initiation, P_C, required to initiate cracks. Figure 4.3 is an optical micrograph of an indent in the alumina sample MT and illustrates the cracks which form at the corners of the indent.

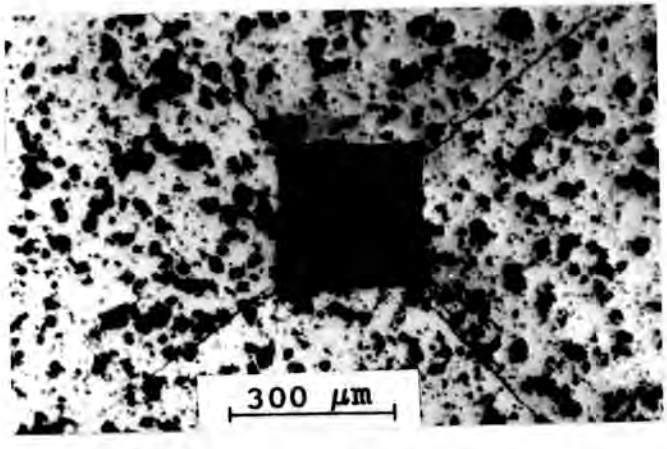

Fig 4.3: The above optical micrograph is of an indent in MT and shows the cracks that form at the corners of the indent.

The length of these cracks can be related empirically to toughness (7 & 43-47). Through the following equations.

Evans and Charles (44) found that at large values of c/a:

$$K_{IC} = 0.1777 H_V a^2 / c^{3/2}$$

$$K_{IC} = 0.0824 P / c^{3/2} \qquad (H_V = 0.4636 P / a^2)$$

where P = load
c = crack length from centre of indent
a = diagonal length of indent.

The fracture toughness of the ceramics were measured by indenting the samples with 50 kgf, except for the basalt and the MD where a 30 kgf was used, and using the above formula. The fracture toughness was taken as an average of three readings which gave a standard deviation of less than 10%. It has not been possible to compare the results with other workers results since no information is available on the fracture toughness of these specific ceramics. The results do however fall within the general region for ceramics and can be found in table 3.1.

4.7 HARDNESS

The hardness of the materials were measured using a Vickers 20 kgf as this load was below the critical load, for crack initiation, for all the materials, except glass, which was measured at a load of 200 gf. The hardness was taken as the average of four tests and are shown in table 3.1.

4.8 ETCHING

There are numerous different chemical and thermal methods available for the etching of ceramics (48), which show up different aspects of the microstructure. The thermal etching method was chosen for etching the grain boundaries of the ceramics. The ceramic was placed in the furnace at the desired temperature for a specified time and then prepared for SEM examination, and micrographs of the microstructure were taken in order to determine grain sizes of the different aluminas. The conditions used for the different grades of alumina are shown in table 4.2

Alumina %	Time hrs	Temperature °C	grain size microns
M99	5.5	1500	2.51
90%JAP	2.5	1400	3.24
M97F	4.5	1350	3.27
M94F	3.0	1450	3.33
M97	4.5	1350	3.86
M94	3.0	1450	3.97
87%US	2.5	1400	4.14
MT	2.5	1400	4.14
90%GERM	2.5	1400	4.75

Table 4.2: The table shows the etching times and temperatures for the various grades of alumina as well as grain size.

Chemical etching techniques using Murakami's reagent, which is a 10% potassium hydroxide, 10% potassium feric cyanide solution, was used for the etching of the tungsten carbides. The specimens were placed in the solution for three minutes at room temperature. The basalt was also chemically etched using Kellers reagent, 95ml water 2.5ml HNO_3 1.5ml 36% HCl and 1ml

40% HF.

Lineal analysis was used on SEM micrographs to give an estimate of the grain sizes of the various high percentage aluminas. An average of 250 grains was taken as the grain size.

CHAPTER 5

RESULTS

All the materials were tested under similar conditions, shown in chapter 4, at the different angles of impingement. A summary of the steady state erosion rates of the various materials at the different angles is listed below in table 5.1. The data listed below has been corrected as discussed in section 4.5.

MATERIAL	EROSION RATE cm^3/g ($*10^{-5}$)			
	90°	60°	45°	30°
BASALT	49.24	23.61	11.02	7.59
ALUMINAS				
MD	53.22	26.05	9.98	5.68
MZF	1.71	1.38	0.77	0.54
M97F	1.62	1.53	0.68	0.54
M97	2.59	2.32	0.82	0.56
M94	2.35	1.97	0.96	0.56
M94F	1.44	1.08	0.61	0.39
M99	1.42	1.31	0.62	0.52
90%JAP	1.00	0.90	0.51	0.31
MT	2.84	2.45	0.95	0.67
87%US	2.01	1.83	0.69	0.53
90%GERM	3.89	3.31	1.79	1.40
GLASS	123.59	54.52	30.08	15.70
6%Co-WC	0.16	0.22	0.14	0.09
10%Co-WC	0.41	0.48	0.29	0.15

Table 5.1: Corrected erosion rates of the materials for the different angles.

A summary of the erosion results for the different angles,

erodents, grit sizes and velocities can be found in appendix 1 showing both the corrected and the uncorrected erosion rates. In all graphs and diagrams the corrected erosion results have been used.

The following three graphs, figures 5.1 to 5.3, show cumulative volume loss vs cumulative mass of erodent at the four different angles for three different materials.

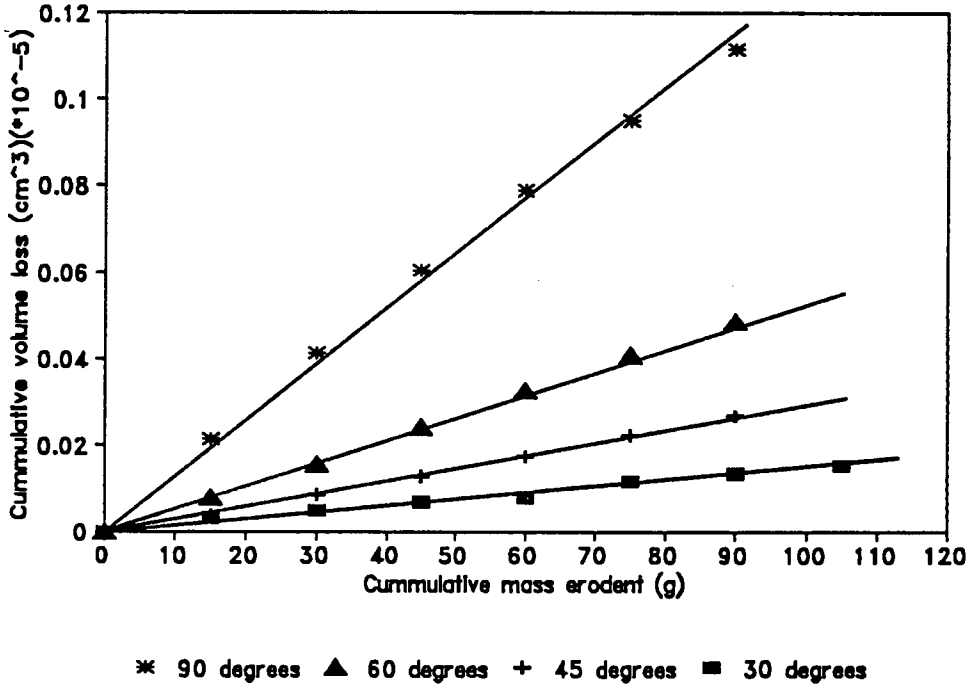

Fig 5.1: Cumulative volume loss vs mass erodent for glass.

Unlike the solid particle erosion of metals particle embedment does not occur to any great extent during the solid particle erosion of ceramics, or show an incubation period prior to mass loss. The tungsten carbide cobalt cermets did however have a small incubation period and the erosion rates were calculated from the region of steady state erosion using linear regression.

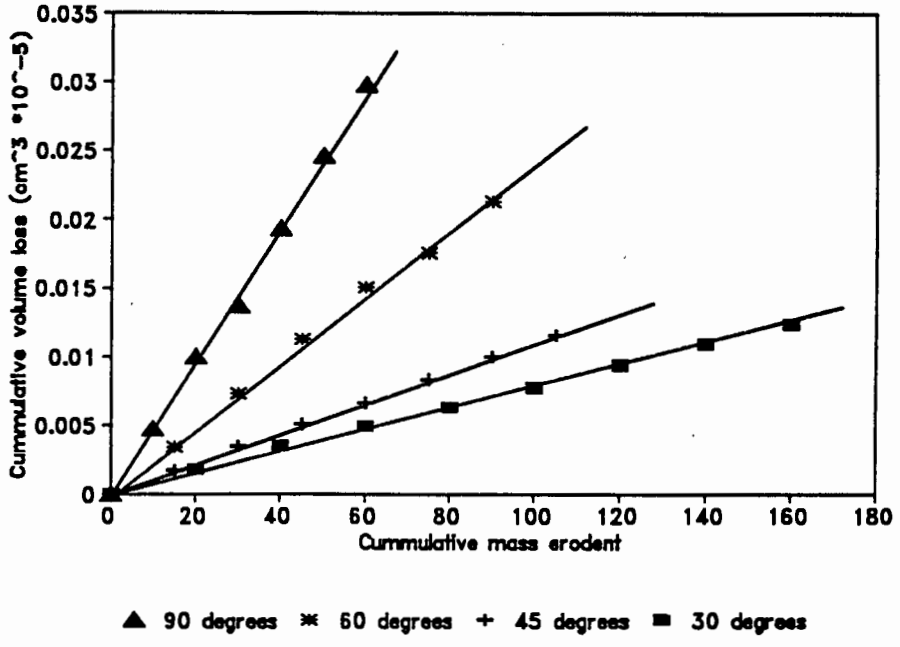

Fig 5.2: Cumulative volume loss vs mass erodent for basalt.

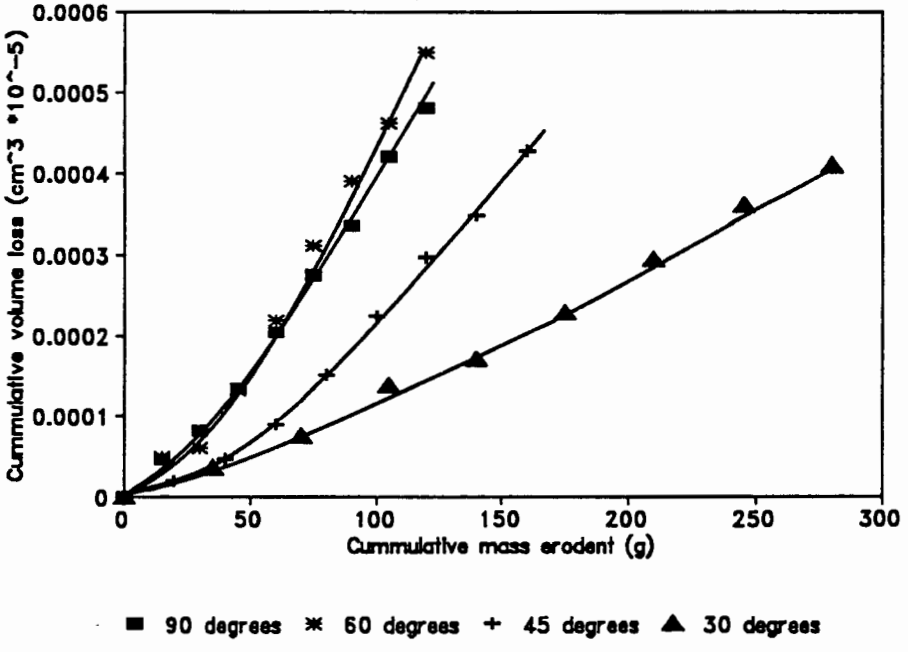

Fig 5.3: Cumulative volume loss vs mass erodent for 10%Co-WC.

There is a high degree of linearity in the graphs of the basalt and the glass while the steady state region of the

graph of the cermet has a lower degree of linearity. It should be noticed that the cermet has very small volume losses, about 50 times lower than that of the basalt. This low mass loss increases the percentage error due to the accuracy available from the balance, which was 0.1mg. Nevertheless reproducibility tests, shown in appendix 4, gave variations of less than 8%

When the materials were ranked with respect to their erosion resistance it was found that there was a very specific ordering at all four test angles, with the exception of the MZF whose respective ranking position changed dependent on the angle of erosive attack. This had the effect of altering the ranking of other materials, see table 5.2.

Material	90°	60°	45°	30°
6%Co-WC	1	1	1	1
10%Co-WC	2	2	2	2
90%JAP	3	3	3	3
M94F	5	4	4	4
M99	4	5	5	5
M97F	6	7	6	6
MZF**	7	6	8	8
87%US	8	8	7	7
M94	9	9	11	9
M97	10	10	9	10
MT	11	11	10	11
90%Germ	12	12	12	12
BASALT	13	13	14	14
MD	14	14	13	13
GLASS	15	15	15	15

*Table 5.2: The ranking of the materials, ** Zirconia toughened alumina.*

However, it can be seen from the above table that if MZF were to be removed the ranking of all the materials would be extremely consistent regardless of the angle of erosion.

The two tungsten carbide cobalt samples were the most erosion resistant of the materials tested, while the glass, basalt and MD (50% alumina) were shown to be the least erosion resistant. Glass consistently showed material volume losses, more than twice that of either the basalt or the MD. Furthermore, basalt and MD showed similar erosion rates that were an order of magnitude greater than all the other ceramics materials tested regardless of the angle of impact.

5.1 THE EFFECT OF ANGLE ON EROSION RATE

One objective of the work was to quantify the effect of the angle of particle impact on the erosion rates of candidate pipelining materials. Figure 5.4 illustrates the erosion rates of four different ceramics plotted against the angle of impact. The four materials were chosen since they were considered to be a representative sample of the ceramic materials tested. The maximum volume loss occurred at 90° and decreased as the angle of impact was made more oblique.

It appears as though there is a sudden change in slope between 45° and 60° impact, instead of a steady decrease in erosion rate as generally observed for ceramics. This phenomena can be ascribed to velocity threshold effects and the particle shape of the erodents used, which is discused further in section 6.2.

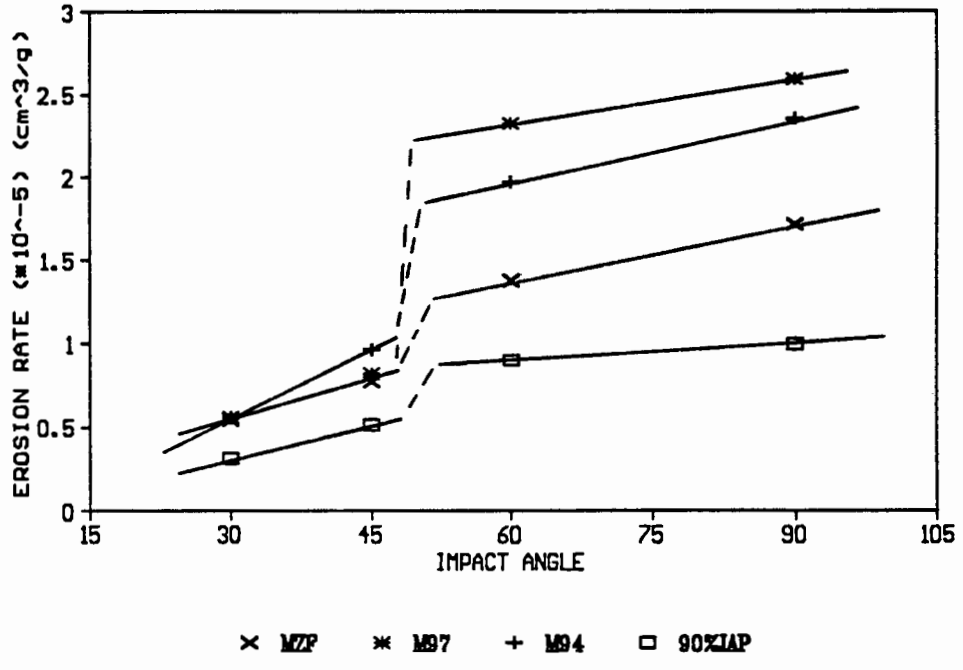

Fig 5.4: Effect of angle on the erosion rate of ceramics.

The two tungsten carbide cobalt cermets on the other hand exhibited a maximum in the erosion rate curve when erosion rate was plotted against angle of impact, see figure 5.5. It was found that the cermet with the higher cobalt content (10%) had a consistently higher erosion rate than the cermet that contained only 6% cobalt binder content.

Unlike ceramics, maximum erosion occurs in the region of 60 degrees which is similar to that shown by ductile materials rather than brittle ceramics. The erosion rate of ductile materials normally shows a maximum in the region of 30°. In the present case there are clearly two competing mechanisms of erosion, one responsible for the loss of the softer binder phase cobalt and the other leading to the loss of the brittle WC, which would explain the shift in the maximum erosion rate from 30° to 60°.

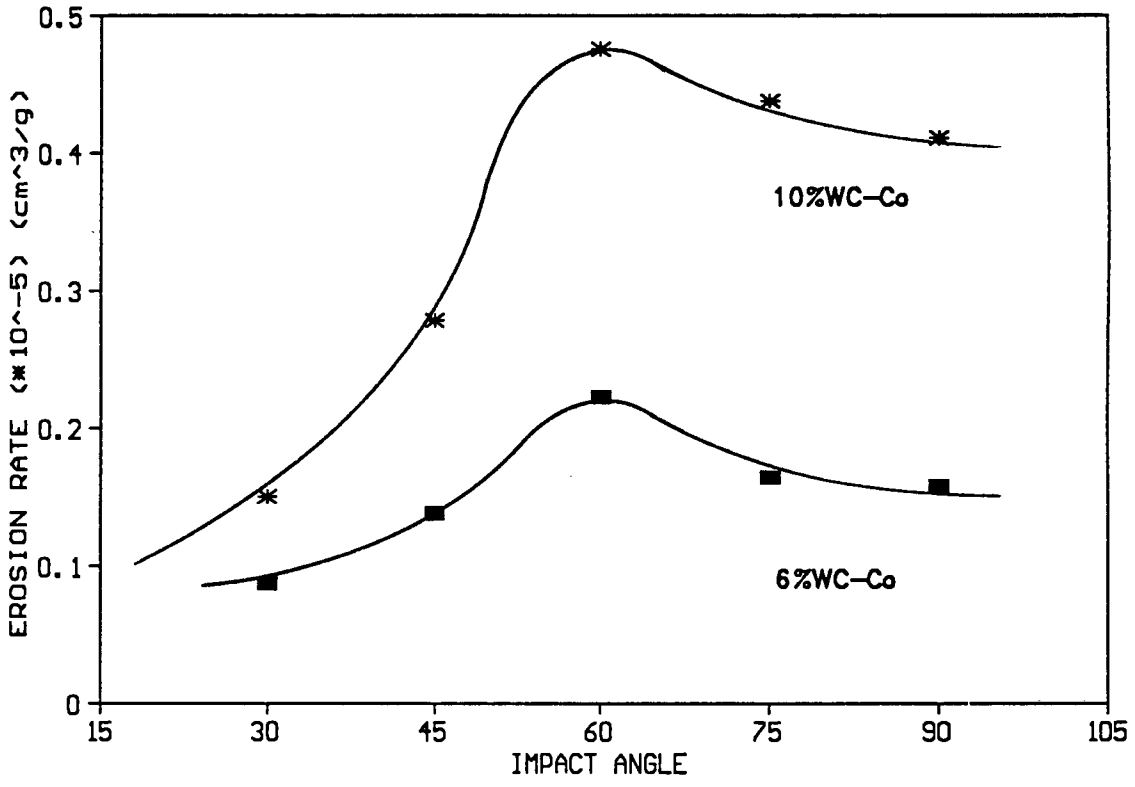

Fig 5.5: Effect of angle on the erosion rates of WC-Co cermets.

5.2 THE EFFECT OF ERODENT HARDNESS ON EROSION RATES

The erosion rates of both M94 and M94F were determined at 60° and 40 m/s using three different erodents, SiO_2, Al_2O_3 and SiC. In all cases 120 grit particles were used. The effects of the ratio of target hardness to erodent hardness is shown in figure 5.6. The 94% aluminas were chosen for further testing since it was available with two different grain sizes and was the most erosion resistant locally produced ceramic. The grain sizes were 3.33 microns and 3.97 microns.

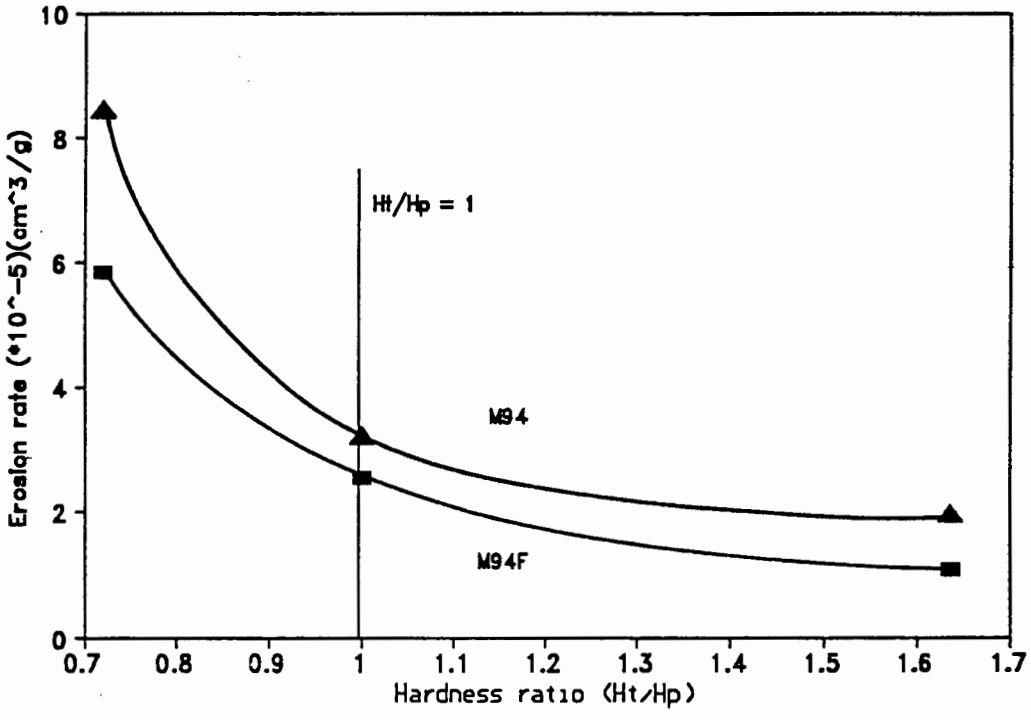

Fig 5.6: Erosion rates of M94 and M94F vs Ht/Hp ratios

When the erodent particles are slightly harder than the target material the erosion rates are relatively high. As the Ht/Hp ratio increases there is a significant decrease in erosion rate to a hardness ratio of unity after which the there is only a slight decrease in the erosion rate. The erosion rates of the fine grained alumina is consistently lower than that of the other 94% alumina.

5.3 THE EFFECTS OF PARTICLE VELOCITY ON EROSION RATES

In order to determine the effect of particle velocity on the erosion rates of ceramics, M94 and M94F were eroded under standard conditions at different velocities, 30 m/s, 40 m/s, 50 m/s and 60 m/s, and the angle of impact was maintained at 60°.

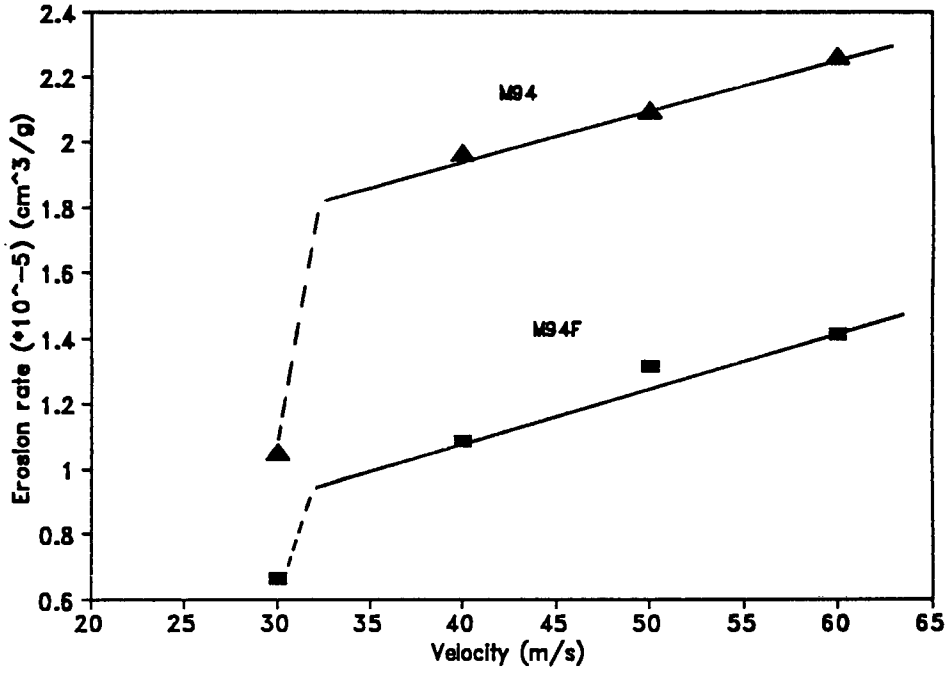

Fig 5.7: Erosion rate vs particle velocity.

Figure 5.7 shows the manner in which the erosion rate increases as the particle velocity increases. A sudden increase in erosion rate is observed at a particle velocity between 30 m/s and 40 m/s after which the erosion rate increases at a constant rate. This sudden increases is ascribed to threshold effects and particle shape and is further discused in section 6.2.

5.4 THE EFFECT OF PARTICLE SIZE ON EROSION RATE

The alumina grades M94 and M94F were used to determine particle size effects on erosion. Both samples were eroded with three different sizes of SiO_2, 100 grit, 120 grit and less than 140 grit. The velocity of impact was kept at 40 m/s in all cases and the angle of impact was maintained at 60°.

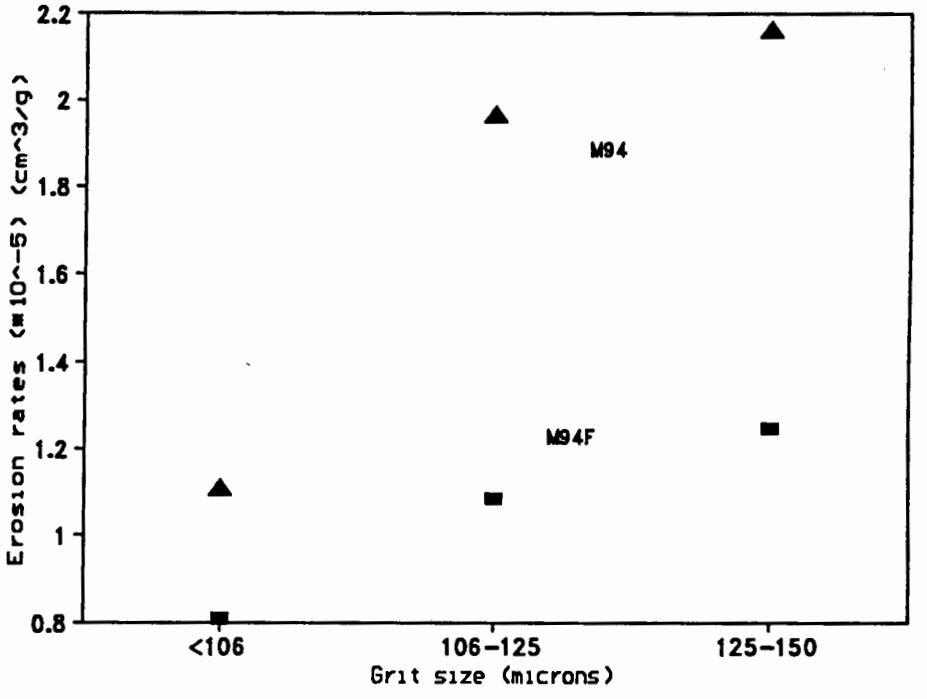

Fig 5.8: Erosion rates vs erodent particle size.

M94 had an erosion rate 80% higher than the M94F when eroded with the two larger particle sizes. This difference dropped to 50% for the smaller 140 grit erodent. The non-linearity of the erosion rate against grit size was probably due to the fact that the 140 grit erodent contained a wider range of particle sizes, from 106μm to about 2μm, than the size ranges shown by the larger erodent grits. These smaller particles are far less erosive and hence a lower erosion rate is likely than would be the case if eroding with a corresponding grit size range between 106μm and 75μm.

5.5 EFFECT OF K_{IC} ON EROSION RATE

Figure 5.9 illustrates the relationship between the fracture toughness of a material and its erosion resistance.

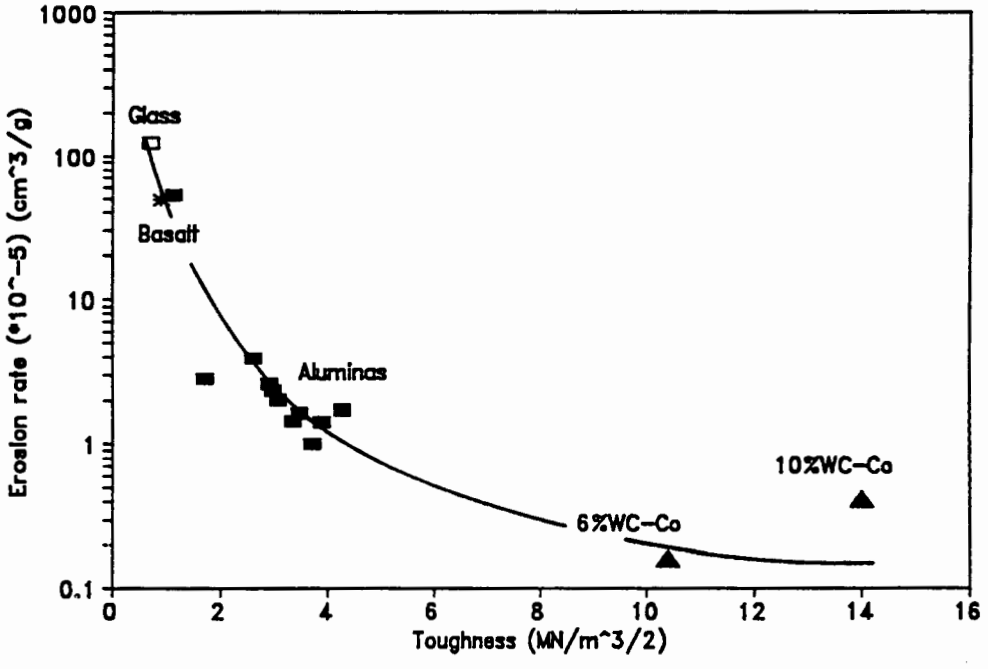

Fig 5.9: The steady state erosion rates of the materials plotted against fracture toughness.

There is clearly a significant decrease in the erosion rate with an increase in fracture toughness for all the materials this decrease however is not linear. The erosion rate for the aluminas decreases significantly as the fracture toughness increases from 0.9 to 4.5 $MN/m^{3/2}$.

The tungsten carbide cermets show an increase in erosion rate with an increasing fracture toughness. This behaviour can be attributed to the fact that by increasing the percentage cobalt, a relatively soft and ductile material, the fracture toughness increases but the erosion rate also increases since cobalt has a higher erosion rate than tungsten carbide.

A plot of steady state erosion rate against the inverse fracture toughness for the high percentage alumina materials yields a straight line graph, see figure 5.10.

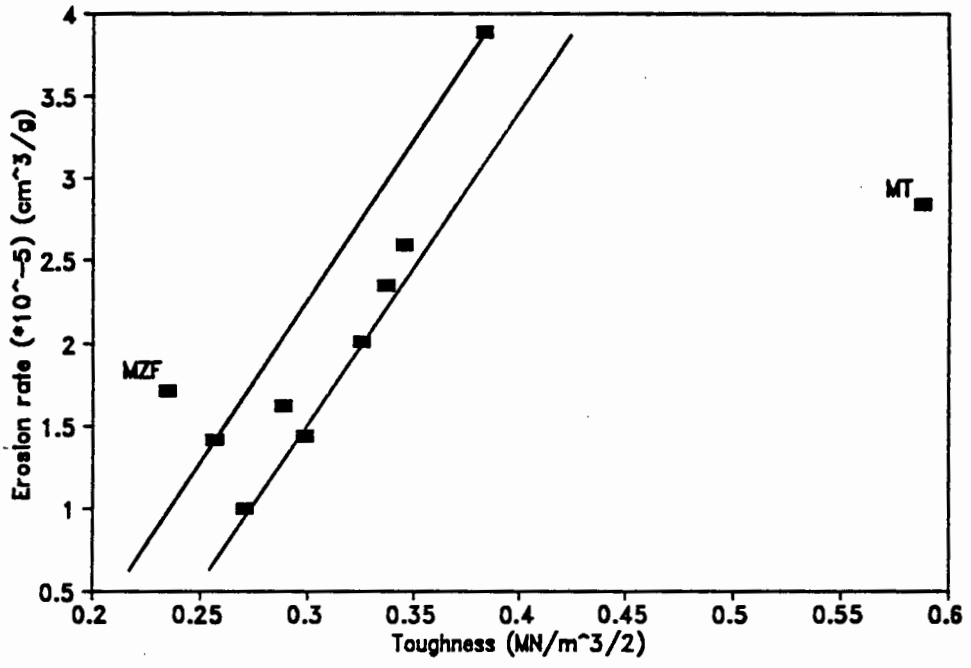

Fig 5.10: Steady state erosion rate vs inverse fracture toughness for high percentage alumina ceramics.

MT, a 90% alumina, had a fracture toughness far lower than expected for a 90% alumina, ca 50% lower. Hence in both graphs there is a point which does not fit the general trend. No explanation for this anomaly of a low fracture toughness can be given at this time.

5.6 EFFECT OF MODULUS OF RUPTURE (MOR) ON EROSION RATE

Erosion rate as a function of the modulus of rupture (MOR) for the different materials is shown in figure 5.11. A similar trend to that shown previously for fracture toughness is obtained, with the two cermets fitting the trend.

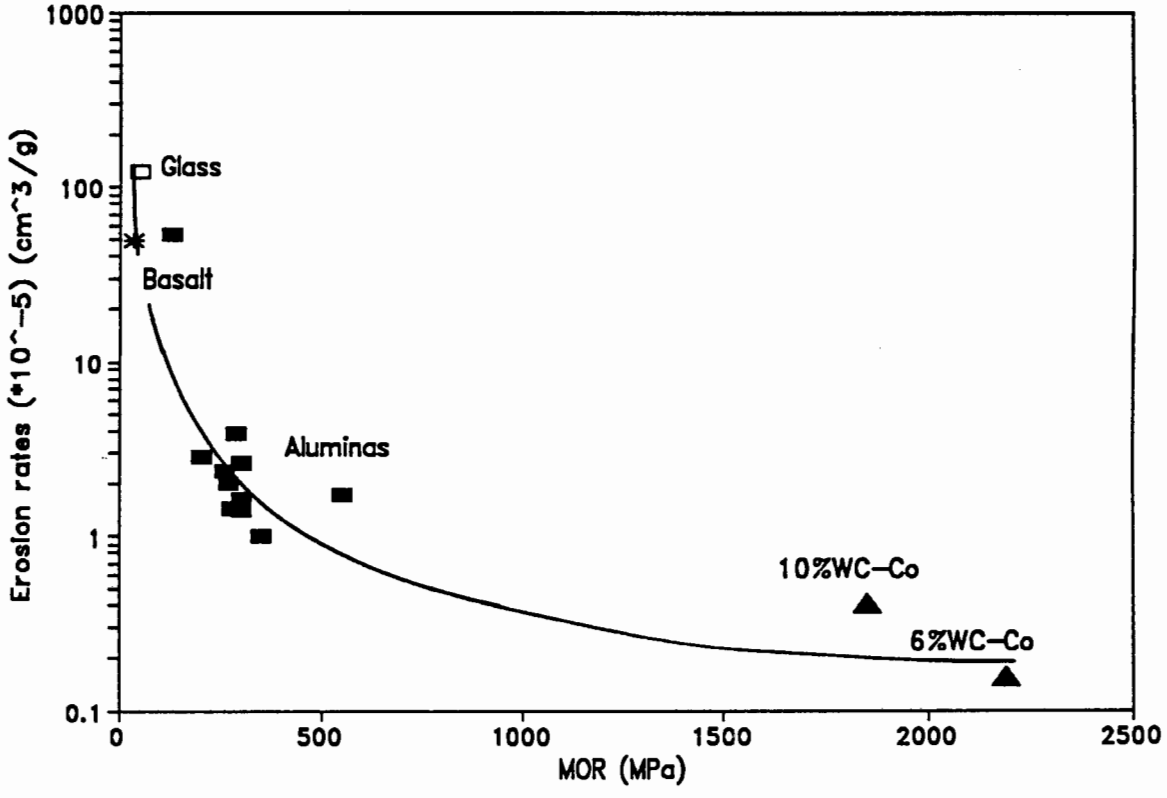

Fig 5.11: Erosion rate verse modulus of rupture for the different materials.

There is a parabolic decrease in erosion rate with an increasing MOR. The greatest decrease in erosion rate occurred at between 50 MPa and 500 MPa for the aluminas. No apparent trends were observed for an inverse relationship between MOR and erosion rate.

5.7 EFFECT OF GRAIN SIZE ON EROSION RATE

Although a range of materials with widely different grain sizes was not used in these experiments, both the 97% and the 94% alumina materials were supplied with two different grain sizes. From these materials it was established that in all the experiments conducted the material with the finer grain

size had a greater erosion resistance. The difference in erosion rates between the M94 and M94F and between the M97 and the M97F increased from 10% at 30° impact to 50% at 90° impact.

The grain size of the high percentage aluminas were determined, and are listed in table 4.2, and plotted against the erosion rates (fig 5.12) to determine the effect of grain size on erosion rate.

Although there is a wide range of compositions, manufacturing techniques, percentage alumina and mechanical properties between the different ceramics it can still be seen that there is a strong tendency for a large increase in erosion rate with a small increase in grain size.

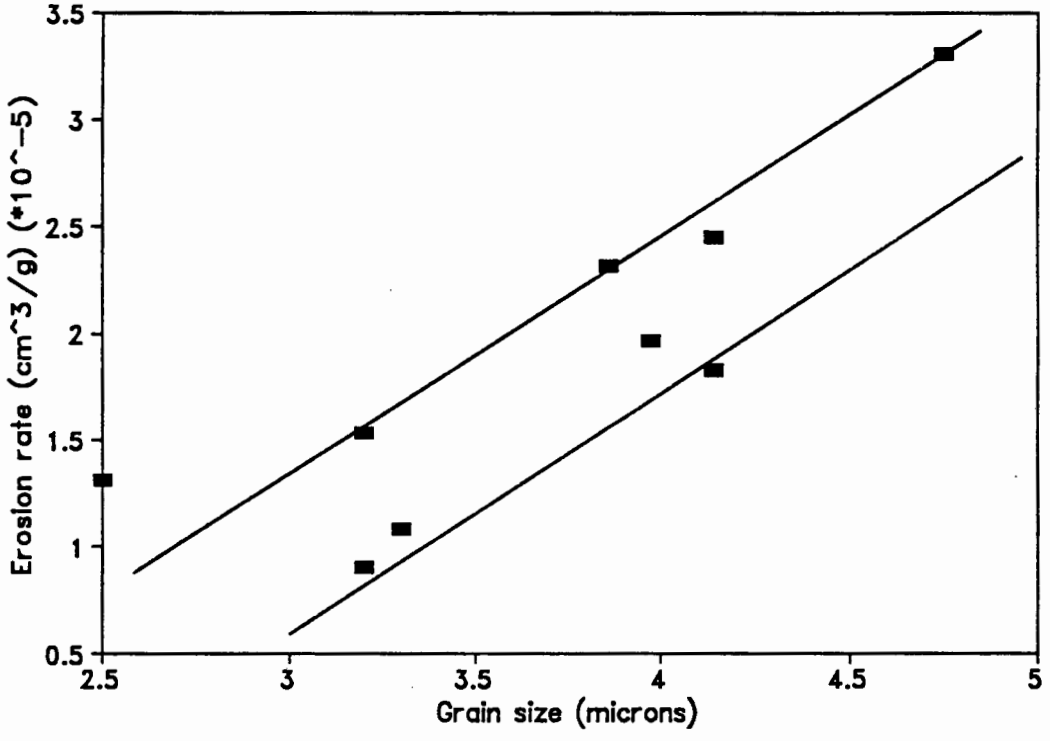

Fig 5.12: The effects of grain size on the erosion rate of ceramics.

5.8 FRACTOGRAPHY OF SINGLE IMPACT SITES

The scanning electron microscope was used to examine single impact sites on the different materials in order to assess the extent of impact damage caused by different conditions, in addition to determining the different modes of erosion. In most cases secondary electron images were used although it was sometimes necessary to use back scattered electrons in order to obtain a better image. While there is a substantial variation in the deformation/fracture pattern for different materials the SEM micrographs chosen were considered to be representative for their conditions.

5.8a BASALT

Figures 5.13 a to d are SEM micrographs of basalt impacted at 90°(a), 60°(b), 45°(c) and 30°(d) by 120 grit SiO_2 particles.

The impact of SiO_2 particles on basalt results in a region of elastic/plastic deformation with varying degrees of cracking. The cracks seem to develop from beneath the region of elastic/plastic deformation and propagate parallel to the surface for a short way before intersecting with the surface to form a chip of material, in the manner of median/lateral cracks. Subsequent impacts on or near these sites can then remove these chips of material from the surface.

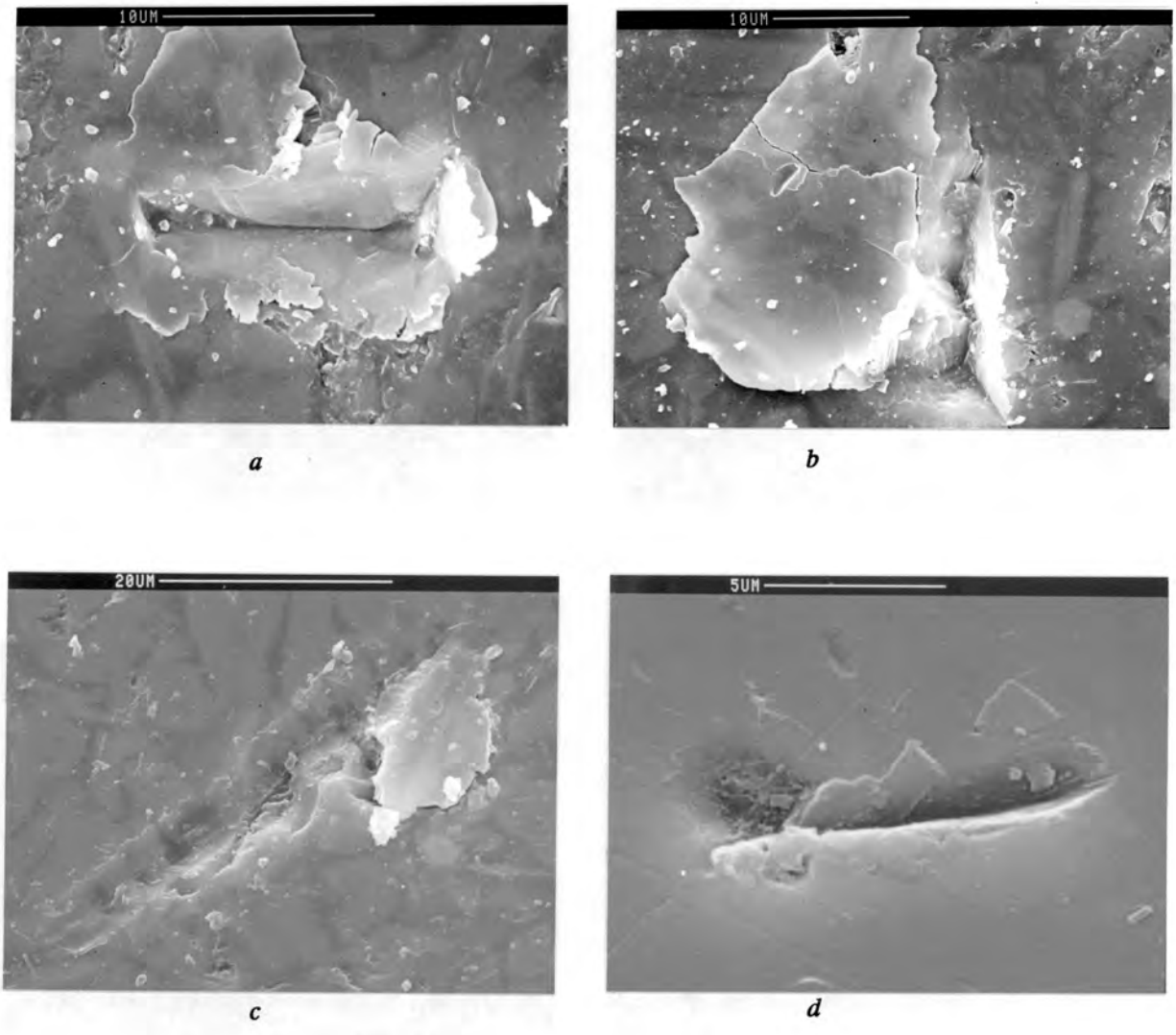

Fig 5.13a-d: Sem micrographs of single impact site in basalt impacted at (a) 90°, (b) 60°, (c) 45° and (d) 30°.

At 60° (a) impact the cracking is slightly extended in the direction of the impact. While at 45° (c) and 30° (d) impact the sites show a very small degree of cracking and the size of the elastic/plastic deformation zone decreases significantly.

5.8b ALUMINA

Aluminas impacted with SiO_2 particles showed an elastic/plastic response with varying degrees of crack formation and extent of the damage zone.

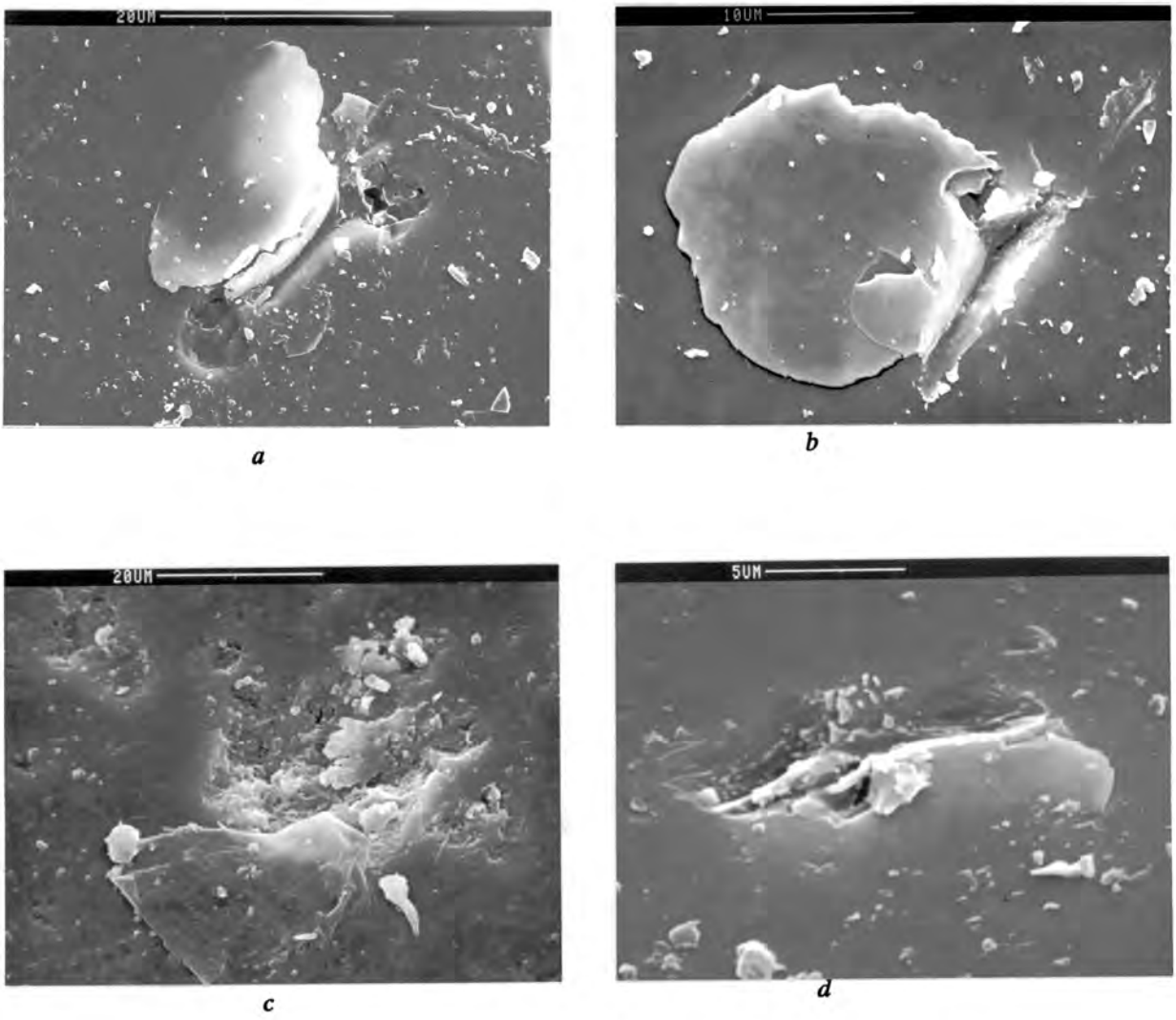

Fig 5.14a-d: Sem micrographs of single impact site in MD impacted at (a) 90°, (b) 60°, (c) 45° and (d) 30°.

At 90° and 60° impact there was evidence of particle fragmentation and debris can be clearly seen on the surface of the specimens in figures 5.14a and 5.14b. At these two angles of impact the predominant form of damage was through the

formation of chips brought about by the initiation and propagation of lateral type cracks. At the lower angles of impact, namely 45° and 30°, the elastic/plastic impact zone was the predominant form of impact damage with cracking occurring on a far smaller scale illustrated in figures 5.14c and 5.14d.

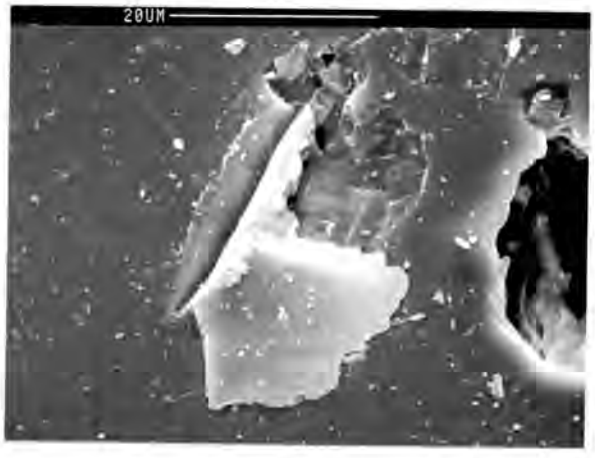

Fig 5.15: Single impact on MD at 90° showing material loss.

Two SEM micrographs of single impact sites on the MD alumina (figs 5.14a & 5.15) clearly illustrate the mechanism of material removal that predominated in these experiments. Figure 5.14a shows evidence of subsurface cracking intersecting with the surface, indicating the possible formation of lateral cracking. Figure 5.15 confirms this assumption, a chip of material has been removed from the impact site and it can be seen that a crack initiating beneath the impact site propagated outwards and upwards to intersect with the surface in the manner of a lateral crack.

5.8c TUNGSTEN CARBIDE

Due to the presence of the ductile cobalt phase in the cermet,

single impact sites show a large region of plastic deformation and associated extrusion lips. The size of the plastic zone and extrusion lips decreases with decreasing angle of impact.

At 90° impact (figure 5.16a) extrusion has occurred and the WC grains have been displaced. The extruded material is then vulnerable to subsequent impacts which could remove material from the surface of the cermet. At 60° impact (figure 5.16b) the damage zone is slightly larger and material removal has occurred in what appears to be a cutting mode.

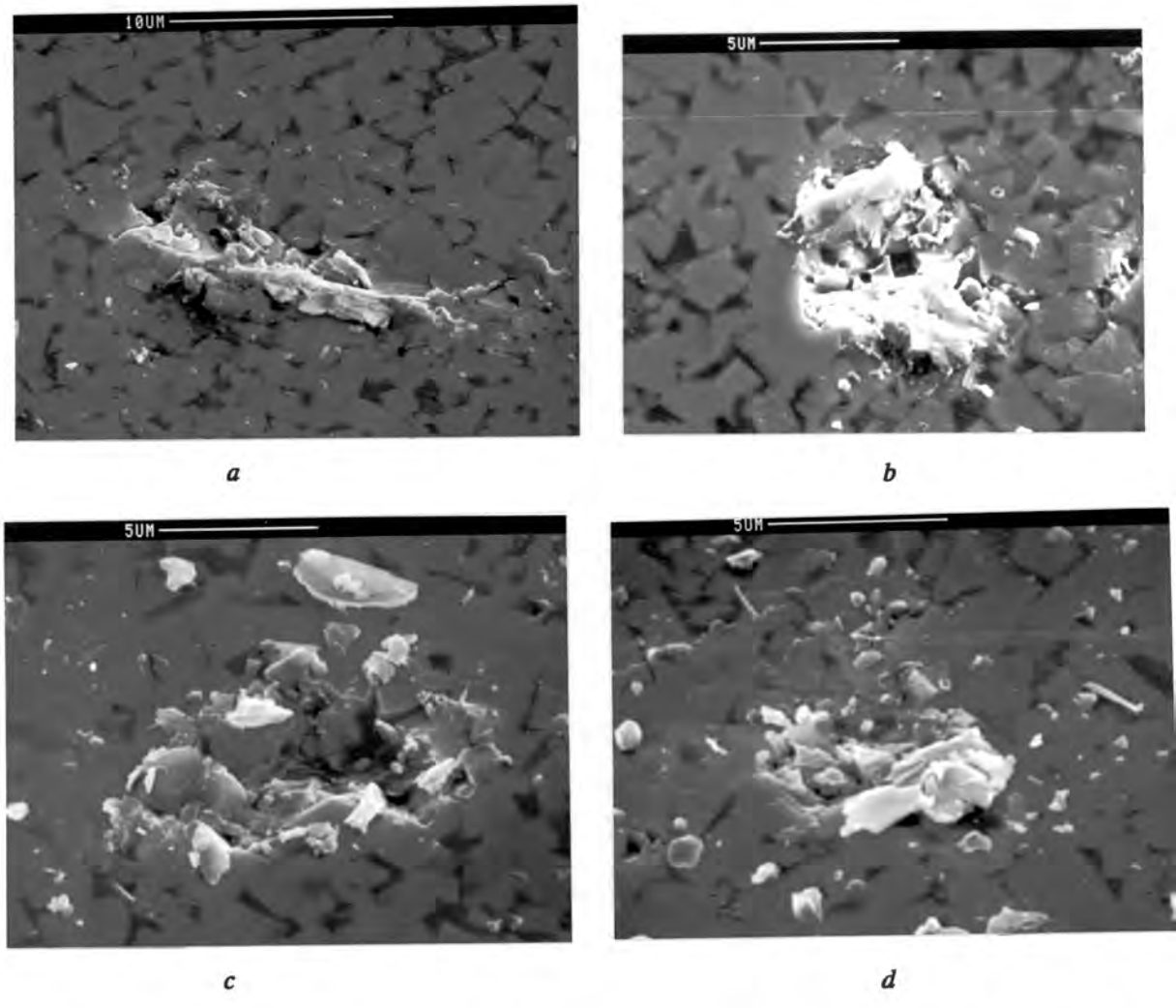

Fig 5.16 a-d: Sem micrographs of single impact site in tungsten carbide-cobalt impacted at (a) 90°, (b) 60°, (C) 45° and (d) 30°.

The impact at 45° (figure 5.16c) has plastically deformed the cermet and the impact site is narrow and elongated in the direction of the impact. The impact at 30° (figure 5.16d) shows extrusion of the cermet in the direction of the impact. At both 30° and 45° impact the degree of WC grain displacement is far lower than the amount of displacement at 60° and 90° impact.

5.8d GLASS

The glass sample did not exhibit the same response to impact angle as the ceramics or the tungsten carbide-cobalt specimens. The lateral crack mechanism predominated at all four angles of impact with very little evidence of plastic deformation.

At 90° and 60° impact the semi-circular arrest bands are visible on the fracture surface. The cracks initiated from beneath a central region of crushed material propagating downwards into the material before curving up to intersect with the surface causing material loss.

There was a marked tendency for the elongation of the crack in the direction of the impact at the lower angles of impact, namely 45° and 30°. This can be observed in figures 5.17c & d. This phenomena was also observed by Wiederhorn and co-workers (34) who stated that the damage caused by impact at an oblique angle shows a marked tendency to elongation along the surface direction containing the plane of incidence. They further stated that the horizontal velocity component may well augment the crack driving forces.

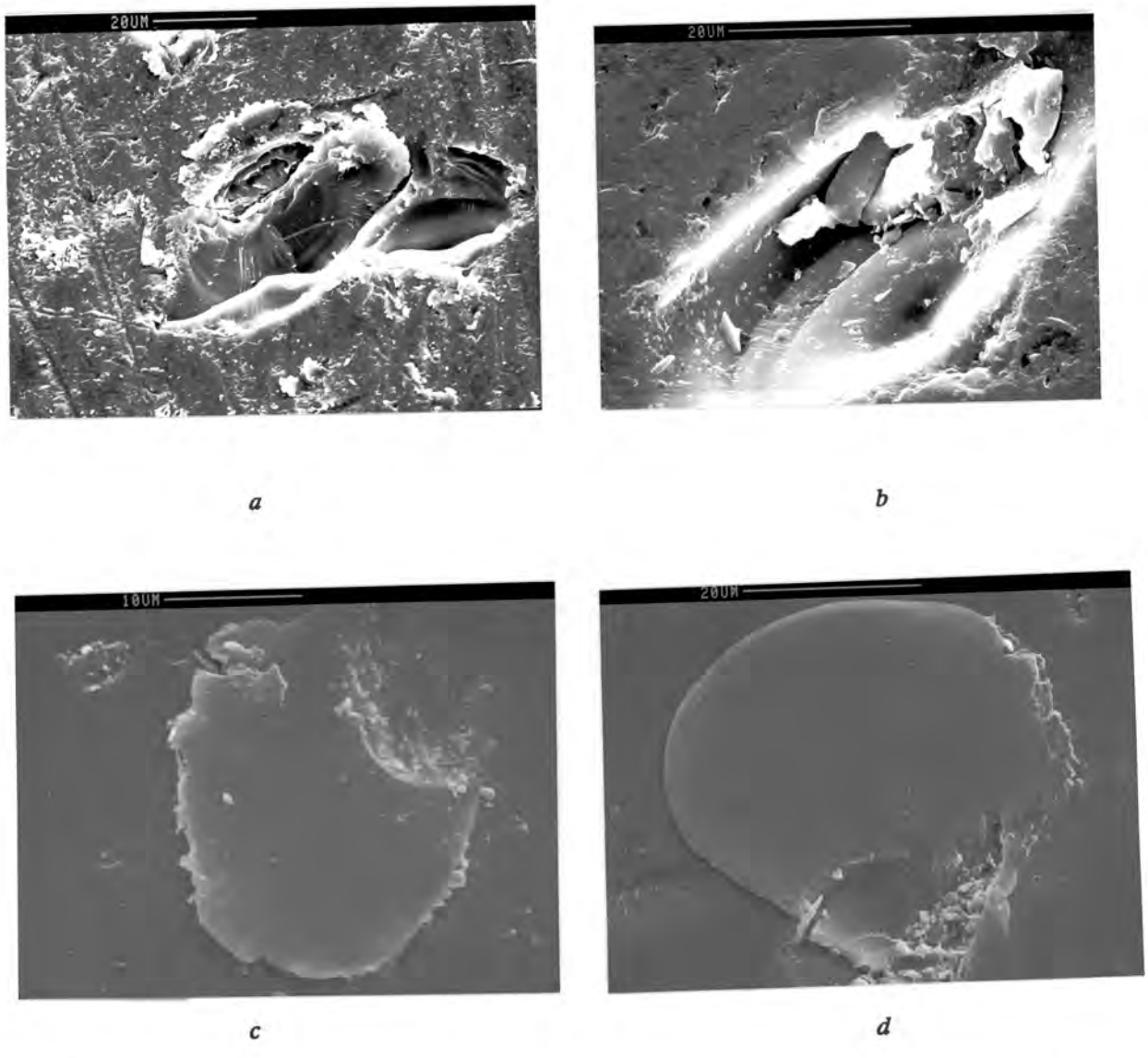

Fig 5.17 a-d: Sem micrographs of single impact site in glass impacted at (a) 90°, (b) 60°, (c) 45° and (d) 30°.

5.9 EFFECT OF PORES ON EROSION OF BRITTLE MATERIALS

The two SEM micrographs in figure 5.18 show the two effects that pores can have on erosion rates of brittle materials. Figure 5.18a is a micrograph of a single impact on a semi-exposed pore on M97F. Extensive cracking has occurred in the material above the unexposed section of the pore and one of

the surface cracks has extended away from the pore. The other cracks have been stopped from further propagation by intersecting with the exposed region of the pore which effectively blunts the crack. The second micrograph figure 5.18b is of the same site at a lower magnification and illustrates the way in which the other crack has been stopped by intersection with another pore.

The only two materials that had a high degree of porosity were MD and basalt both of which had a high erosion rate. However this can not be attributed to the porosity alone since they both also had a low hardness, MOR and fracture toughness. The other materials all had very low degrees of porosity. This makes it difficult to comment conclusively on the effects of the degree of porosity on the erosion rate of a material.

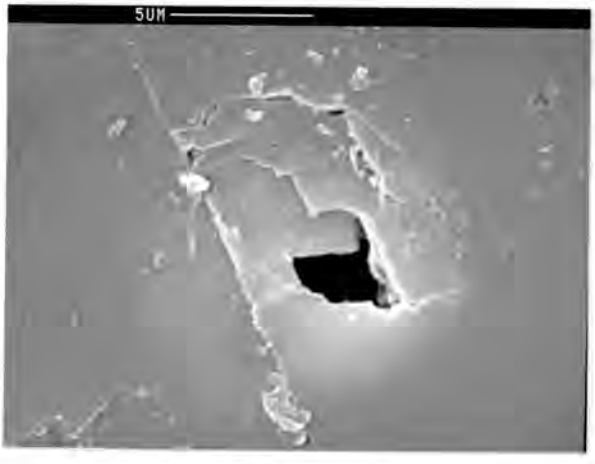

Fig 5.18a:

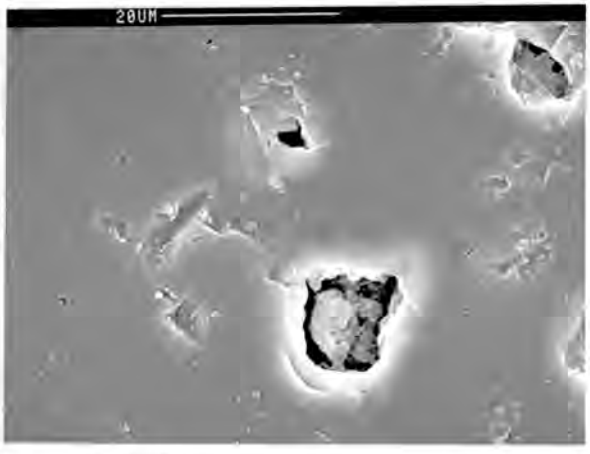

Fig 5.18b:

Fig 5.18a & b: SEM micrograph of single impact site on subsurface pore.

5.10 ERODENT FRACTOGRAPHY

Since 90% of the experiments were conducted using 120 grit SiO_2 particles it was decided to examine the particles after impact. As mentioned previously, silica is an extremely

friable material and one can see this in the SEM micrograph, Figure 5.19, of the used particles. As can be seen the silica suffers from large scale fragmentation after impact.

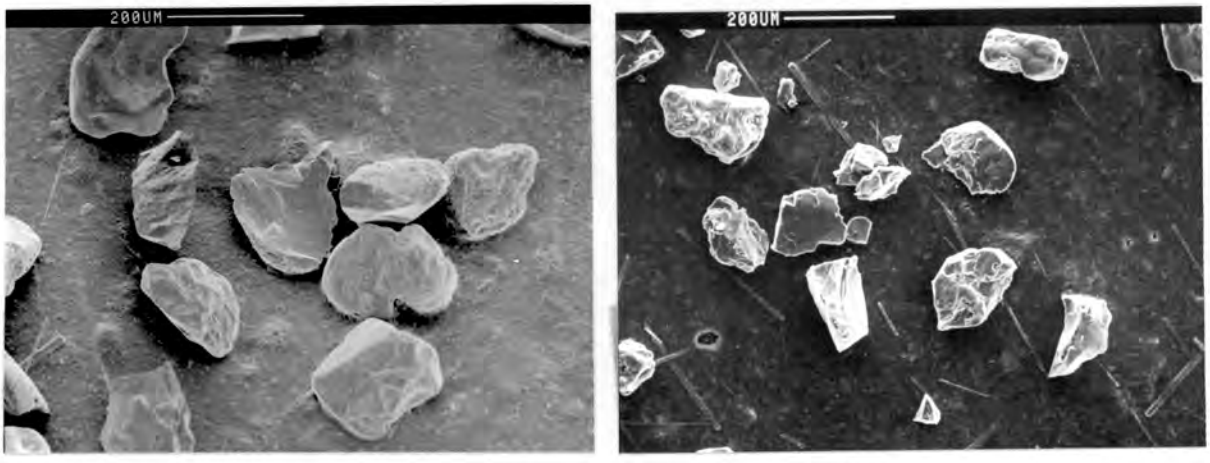

a) b)

Fig 5.19: SEM micrograph of the 120 grit SiO_2 particles a: before impact and b: after impact on M94 at 90°.

CHAPTER 6

DISCUSSION

In the present work a variety of different materials have been subjected to solid particle impact erosion. The loss of material has been found to be dependent on the relative properties of the impacting particles with respect to those of the target. Twelve possible responses have been enumerated by Vaughan and are shown in table 6.1 and illustrated in figure 6.1. Using this classification it has been possible to divide the fifteen different materials into three groups.

The first group is the material which showed a purely brittle response namely glass. The second group, the largest, contains all the ceramics which showed various degrees of plastic deformation and fracture. The last group consists of the two Co-WC cermets which had an almost ductile response to solid particle impact.

Material loss during solid particle erosion of the aluminas was found to be via a process of dynamic elastic/plastic loading and associated plastic deformation and lateral fracture. Material removal occurred through the interaction of the lateral cracks with each other and the surface of the target causing the loss of chips of material. In many cases damage accumulation was necessary before lateral fracture could occur.

The glass showed a brittle response to impact with no plastic deformation visible. Crack initiation occurred beneath a region of crushed material. The two cermets showed a plastic response with no evidence of brittle fracture.

Each of these groups are discussed separately and more fully in the following sections. Important factors affecting erosion rates are also discussed.

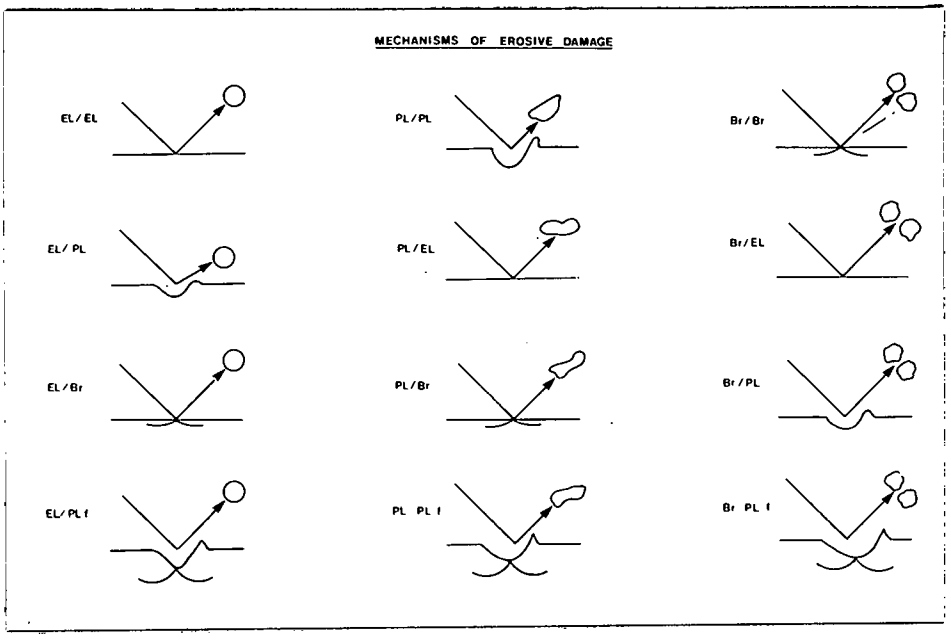

Fig 6.1: The twelve responses of a ceramic or ultrahard material to solid particle impact. (El = elastic; Pl = plastic; Br = brittle; f = fracture)

	Target properties			
Erodent properties	Hard Tough	Hard Brittle	Soft Tough	Soft Brittle
Hard, tough	El/El	El/Br	El/Pl	El/Pl,fr
Hard, brittle	Br/El	Br/Br	Br/Pl	Br/Pl,fr
Soft, tough	Pl/El	Pl/Br	Pl/Pl	Pl/Pl,fr

Table 6.1: The twelve responses of a ceramic or ultrahard material to solid particle impact. (El = elastic; Pl = plastic; Br = brittle; fr = fracture)

6.1a GLASS

The damage morphology produced on the glass surface by the SiO_2 particles showed the classical features of quasistatic indentor patterns (10 & 49) with the only obvious variants due to geometrical variations in the particles themselves. The most conspicuous damage is the surface spalling attributed to the lateral cracks and a central zone of damaged (crushed) material.

At all angles of impact the glass showed a purely brittle response with no evidence of plasticity. Cracks initiated beneath this central zone of crushed material and propagated radially downwards and outwards then turning upwards to intersect with the surface expelling a chip of material.

At the higher angles of impact semi-circular arrest bands are visible where the chip of material has been removed. As the angle of impact decreased there was a tendency for crack elongation in the direction of the impact as is evident in figures 5.17c & d. This as discussed in section 5.8d is attributed to the vertical component of the impact vector.

6.1b CO-WC CERMETS

A low cobalt content in these cermets results in the development of a rigid "skeleton" of WC grains. When an impacting particle strikes the surface, the load is transferred across the rigid "skeleton" structure, resulting in little grain fracture. The formation of the impact site is due mainly to the extrusion of cobalt and the displacement of the WC grains, as illustrated in figures 5.16a-d.

Studies on the erosion of the Co-WC alloys by hard particles show that depending on the erosion conditions the behaviour

may change from a brittle mode, where the maximum erosion occurs at normal impact, to one resembling a ductile material, where maximum erosion occurs at an oblique angle (19 & 50-52).

In this case the maximum erosion rate of the alloys occurs in the region of 60° impact, which also show the greatest amount of damage and extrusion. At all angles of impact, material loss appeared to occur predominantly via an extrusion mechanism with no definite evidence of fracture in the WC grains.

Although not observed, the possibility of fracture in the WC grains can not be ruled out. However, any fracture occurring in the WC grains would be confined to one grain due to the presence of the cobalt phase and would hence be extremely small and difficult to observe, but fracture leading to the loss of particles of material would contribute to the over all erosion rate. Debris from the fracture of the SiO_2 particles was observed in the vicinity of most impact sites.

The 10% Co-WC cermet showed a greater increase in erosion rate with increasing particle impact angle up to 60° than the 6% Co-WC sample. At 30° impact there was a 50% difference in erosion rates which increased to a 150% difference at impact angles between 60° and 90°. This phenomena can be attributed to the increase in the cobalt binder phase which facilitates the extrusion process leading to a much greater material loss.

6.1c BASALT AND ALUMINA

The basalt and the aluminas showed the same type of response to solid particle erosion under the conditions used and hence their mechanisms of material loss will be discussed together under the term ceramics.

Erosion of these ceramic materials is due to elastic/plastic indentation characterised by central regions of irreversible plastic deformation with associated median and lateral cracking. The extent of crack propagation is dependent on the residual stress about the indentation due to the mismatch between the plastic zone and the surrounding elastic matrix (53 & 54). Material removal occurs via the interaction of these cracks with each other and the surface forming chips of material which is then lost from the surface.

At high angles of particle impact, the extent of the cracking is greater than that of the particle contact area, while at the lower angles of particle impact, minor cracking occurs on a finer scale than that of the particle impact site. This transition from a fracture-dominated to a plastically-dominated impact response occurs between 45° and 60° and results in a sudden decrease in the erosion rates as illustrated in figure 5.4. As the angle of impact is decreased, the vector of the velocity component perpendicular to the target is reduced. This results in a decrease in transmitted impact energy, and a stage is reached where the stress fields produced by particle impact at an oblique angle is not great enough to initiate lateral cracking. Multiple impacts are then required for the accumulation of deformation necessary to produce the required stress fields for crack initiation.

Although all the ceramics showed the same type of response to solid particle impact, the high percentage aluminas had a far lower erosion rate than the basalt and the MD (the 50% alumina). There are a number of factors which are responsible for the vast difference in erosion rate. The high percentage alumina samples had a much higher hardness than the basalt and the MD both of which had a hardness slightly lower than the SiO_2 erodent. Hence the basalt and MD are subject to a greater degree of plastic deformation leading to a greater

stress in the material. In addition these two materials had a considerably lower fracture toughness than the other aluminas. All of these factors combined to give the Basalt and MD an erosion rate an order of magnitude greater than the other aluminas.

6.2 VELOCITY AND ANGLE EFFECTS

During solid particle erosion of brittle materials a fairly steady decrease in the erosion rate with a decrease in impact angle is expected as illustrated in figure 2.1, and observed by many workers in this field (3, 14 & 30). However, under the conditions used during these experiments, this trend was not observed. As shown in figure 5.4 there was a large increase in the erosion rate of the ceramics when increasing the angle of impact from 45° to 60°. The possibility of another threshold was also observed when examining the effects of velocity on the erosion rate of the two 94% aluminas, which can be seen in figure 5.7. A large increase in erosion rate was observed between 30 m/s and 40 m/s when eroding with 106-125μm silica of a fairly rounded nature. These transitions are ascribed to a change in the erosion mechanism and is discussed later in this section.

These transitions have also been observed by Hutchings (14,56 & 55) and are ascribed to a change in erosion mechanism due to the nature of the erodent. He found that when eroding the ceramics at 44 m/s the rounded particles showed a sharp increase in erosion rate between 45° and 60° while for the angular particles there was no sudden transition observed, figure 6.2. Eroding at 52 m/s, the rounded particles showed no transition to a higher erosion rate and followed a trend similar to that shown by the angular particles.

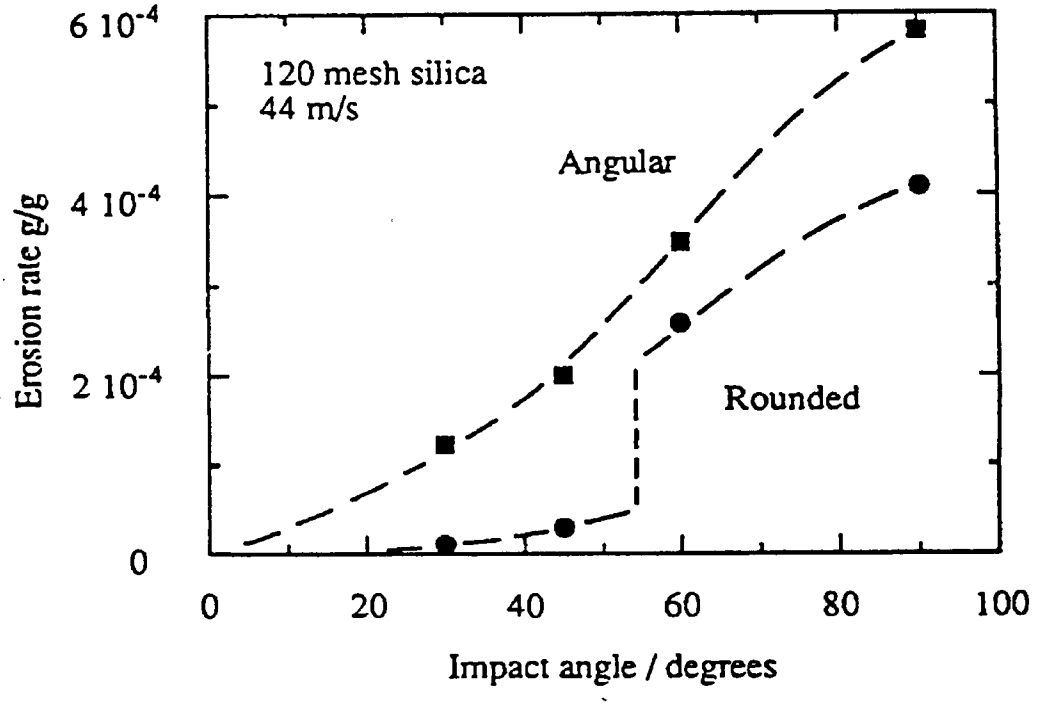

Fig 6.2: Plots of steady state erosion rate against impact angle for a silicate glass-ceramic eroded by silica particles of two different shapes: a) at 44 m/s and b) at 52 m/s. After Hutchings (14).

A similar velocity threshold was also observed by Hutchings (14) who found that eroding silicate glass under similar conditions but using differently shaped particles could result in vastly different responses depending on the velocity of impact. It was observed that when eroding with rounded particles there is a sharp increase in erosion rate with an increase in the velocity of impact from 44 m/s to 52 m/s (14). When eroding with angular particles, this transition did not occur. This phenomena is illustrated in figure 6.3.

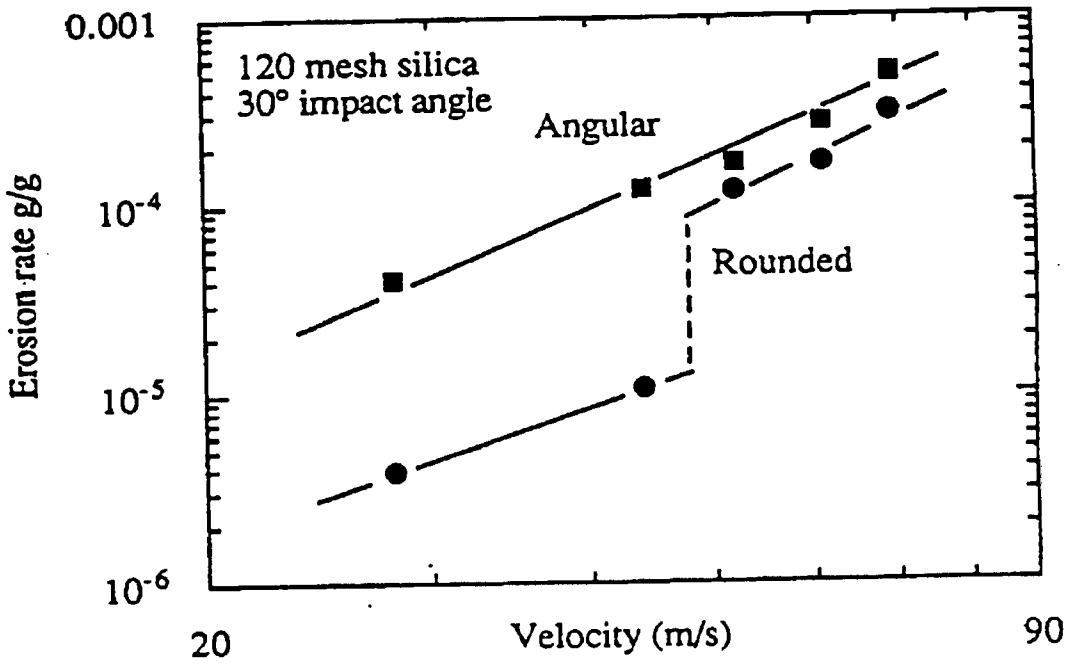

Fig 6.3: Plot of steady state erosion rate against impact velocity for a silicate glass ceramic eroded with two different shapes: angular and rounded (14).

SEM micrographs of single impact sites support the theory that these transition points that are due to a change in the extent and to some degree the nature of the impact damage. When examining single impact sites of alumina it becomes evident that there is a change in the nature of the damage when one compares the higher angle impact sites (90° & 60°) to the lower angle impact sites (45° & 30°). Above the transition point, material removal is via the formation of relatively large flaky fragments formed by lateral fractures associated with the particle impact sites. Below the transition point the impact damage is more plastic in nature and the fracture is much less extensive, with lateral fracture occurring on a small scale at fewer impact sites. Figures 5.14c and 5.14d illustrate these points.

The tungsten carbide-cobalt cermets did not exhibit a

transition point in the manner of the alumina ceramics. Glass showed a steady decrease in erosion rate with corresponding decrease in the impact angle. The tungsten carbide-cobalt cermets on the other hand showed a ductile response to the changes in the impact angle (figure 2.1) with maximum material removal occurring between 45° and 60°, figure 5.5. This behaviour is ascribed to microstructural effects and according to Anand et al (57) is strongly systems dependent, this is discussed further in section 6.3.

6.3 MICROSTRUCTURAL EFFECTS

The role of microstructure on solid particle steady state erosion rate can be quite significant, but it is difficult to quantify, and has never been systematically investigated (56 & 57). Microstructure also plays an important role on fracture resistance which is an important factor in erosion resistance (58).

For given conditions Anand et al (57) found that in the erosion of tungsten carbide-cobalt cermets an order of magnitude increase in erosion rate could be obtained when going from a fine grained alloy (2 micron tungsten carbide grain size) to a coarse grained alloy (16 micron tungsten carbide grain size). The changes depended on erosion conditions and were ascribed to microstructural constraint. Since lateral cracks in the fine grained tungsten carbide particles could not traverse to their full extent due to impingement with the cobalt binder, lateral crack controlled erosion was significantly reduced and the overall erosion resistance increased. This behaviour will be observed as long as the microstructural feature size is smaller or comparable to that of the impact site. As can be seen in figures 5.16a to 5.16b in the present case the impact sites are larger than the tungsten carbide grains.

The average defect size in ceramics is usually related to grain size and the largest defects are found in large grained materials. The critical stresses required for lateral initiation will be much smaller in the presence of large defects The probability of crack initiation will increase with increasing defect density.

Both the 94% and the 97% aluminas were supplied in two different grain sizes. In both cases, the samples with the smaller grain size showed a greater erosion resistance. It was also found that the fracture toughness of these aluminas decreased with increasing grain size, which has also been observed elsewhere (58). The aluminas containing a higher alumina content showed a tendency toward an increase in erosion rate with an increase in grain size illustrated in figure 5.12. The trend is rather tenuous but it must be taken into account that the ceramics all have different hardnesses, fracture toughnesses, manufacturing routes and additives. All of these factors will affect the erosion rates of the ceramics. Hence in order to obtain a quantitative measure of the effect of grain size on the erosion rate it will be necessary to use materials where the only variable is the grain size.

6.4 EFFECT OF FRACTURE TOUGHNESS

Since the erosion of brittle ceramics is primarily via a mechanism involving the initiation and propagation of microcracks one expects that the fracture toughness of the material will affect the erosion rate. A plot of the log of erosion rate against fracture toughness, figure 5.9, shows a definite tendency for erosion rate to decrease with increasing fracture toughness for the whole range of ceramic materials tested. Figure 5.10 shows a linear relationship between

erosion rate and the inverse fracture toughness, of the ceramics with a alumina content of > 80%; with erosion rate decreasing as fracture toughness increases. MT is the only material that didn't fit this trend as it had an exceptionally low fracture toughness compared to the other high percentage alumina materials. This decrease in the erosion rates of the ceramics is due to the higher energy needed to initiate and propagate cracks in the target material when there is an increase in the fracture toughness. This effect has also been reported by R.A Vaughan (29 & 30) and Scattergood (57) a similar trend was observed by Evans et al (9) and Wiederhorn et al (15) both of whom plotted erosion rate against $K^{4/3}H^{1/4}$, from an equation predicting volume loss. It has been proposed that it is not the relative hardnesses of the target and particle that control the erosion rate but their relative fracture toughnesses (44) as observed in this work.

The opposite of this trend was observed for the erosion of the tungsten carbide-cobalt cermets which showed an increase in erosion rate with an increase in fracture toughness. This increase is due to an increase in the cobalt content since in order to increase the fracture toughness of the cermet more of the soft ductile cobalt is added, which is less erosion resistant than the tungsten carbide grains.

This increase in the cobalt binder phase increases the degree of extrusion and displacement of the tungsten carbide grains that occurs during solid particle erosion. The more extrusion that occurs, the greater the erosion rate and the tungsten carbide grains, which are the erosion resistant phase of the cermet, are more easily removed from the surface.

6.5 EFFECT OF TARGET AND PARTICLE HARDNESS

Although there was not a direct relationship between erosion rate and target hardness, the target hardness is expected to affect the erosion rate. The target hardness determines the amount of plastic deformation and hence the size and extent of the stress field, which together with the fracture toughness will determine the extent of the lateral cracking and hence material removal in brittle materials.

It was observed that as the ratio of the target hardness to the hardness of the erodent particle approaches unity, there is a sharp transition in the erosion rate. Relatively soft erodents lead to less erosion. It has been suggested that softer erodents can fragment and crush on impact (13, 31). Evidence of this has also been observed in this work. In steady state it appears that the lateral-crack-based erosion mechanism still operates, but for softer erodents and oblique angles damage accumulation is necessary to build up the required stress to produce lateral cracks.

When the erodent hardness is similar to that of the target the ease of crack initiation is the major factor determining erosion rate. In metals which are soft and tough, cracks are initiated in regions of intense localised shear. Lateral cracks initiated in ceramics are nucleated from defects on the elastic/plastic boundary beneath the zone of irreversible plastic deformation.

Particles softer than the target will themselves fracture or plastically deform this requires energy which thus reduces the energy transferred to the target. Multiple impacts are then sometimes required to build up the necessary residual stresses to initiate fracture. These results were in accordance with other authors (13 & 59) who found that when the erodent is softer than the target material the impact sites are very

small and plastic with little cracking.

When the erodent is much harder than the target material, in this case SiC, crack initiation is inevitable and crack propagation is the rate controlling factor. This accounts for the sudden increase in the erosion rates of the 94% aluminas when eroded with SiC (H_t/H_p = 1.64) compared to Al_2O_3 (H_t/H_p =1) and SiO_2 (H_t/H_p = 0.72).

When eroding different target materials with the same erodent the target hardness can not be used as a means of predicting relative erosion rates.

6.6 RELATIVE PERFORMANCE AND COST IN THE CHOICE OF LINING MATERIALS

When choosing a lining material, the cost relative to it's life expectancy is extremely important. It is no good using a material which is twice as erosion resistant than another if it costs 10 times as much. Another important factor to take into account is the downtime needed to line the pipes, this factor is a lot more difficult to quantify. Hence it is important to not only know the erosion resistance of a material but also it's cost relative to other materials.

The basic relative cost of the different materials will determine their feasibility for use as pipeliners. Due to the weak Rand the imported aluminas are all far more expensive than the locally produced equivalents. Unfortunately exact figures are not available for these imported ceramics. The table 6.2 below is of the relative costs of some of the materials. Even though the 90% Japanese produced alumina showed the best erosion resistance of the ceramics tested, between 15% and 40% more resistant than M94F, it costs at least 50% more than the M94F.

ceramic	R/kg
MZF	300
M99	120
M97F	35-65
M97	18-25
M94F	24-35
M94	12-18
MD	8-12
BASALT	6-10

Table 6.2: The relative cost of various ceramic pipelining materials.

The bar chart in figure 6.4 shows the erosion rates at 45° impact of the high percentage alumina ceramics for easy comparison of the different materials.

As is evident in the above table and bar chart that the most erosion resistant locally produced ceramic M99, is four times more expensive than the M94F but only marginally more erosion resistant. At the lower angles of erosion there is less than a 50% difference in the erosion rates of the locally produced high percentage alumina ceramics. The most viable ceramic seems to be M94, although it has a higher erosion rate than the M94F. However the relative cost makes M94 a better option.

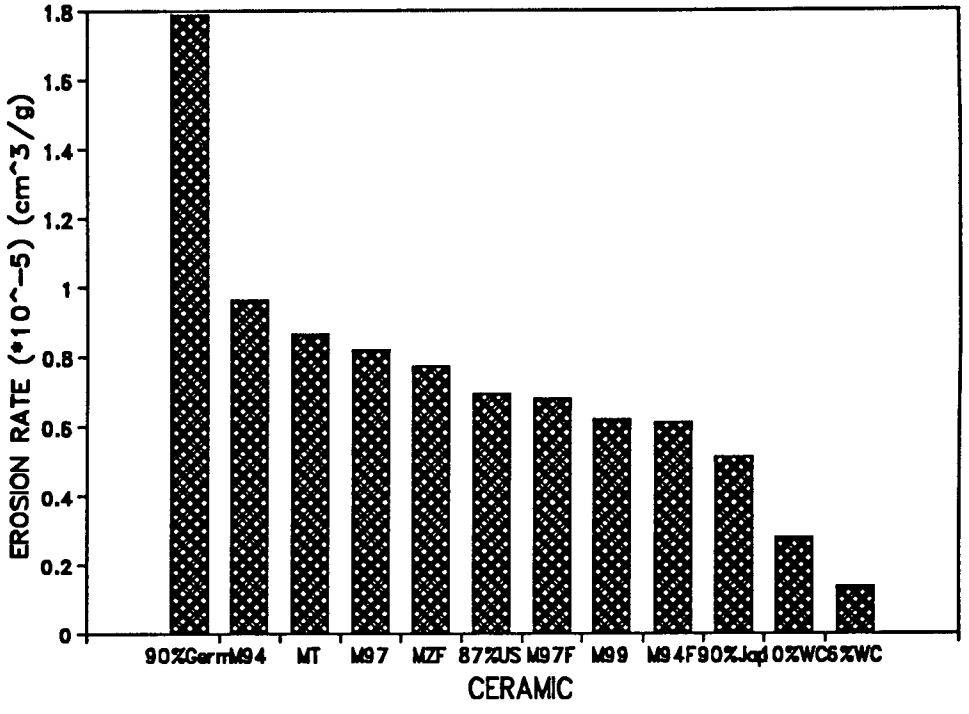

Fig 6.4: Bar chart of the erosion rates of the high alumina content ceramics eroded at 45°.

Basalt and MD can be ruled out as lining materials for the pipe bends since they have excessive erosion rates and are only marginally cheaper than the other ceramics. They are however adequate for the straight sections of the pipe work. Basalt is cheaper than MD but can not be made to as fine a dimensional tolerance as MD and it can not operate at as high a temperature due to spalling.

It would be worth considering lining the different sections of the of the pipes with different materials. For example MD could be used for the straight sections, M94F for the outer radius of the pipe bend and M94 for the inner radius of the pipe bend. Using a composite lining is clearly better than using a more expensive liner where it is not necessarily required.

The use of a 6%Co-WC cermet has to also be considered since this was the most erosion resistant of all the materials tested. The relative cost of the cermets compared to the ceramics was difficult to obtain and has been estimated to be between 4 and 6 times as expensive as the M94. It did however have an erosion rate approximately 25% of that of M94F. There are other factors which make the use of a cermet more complicated. It is extremely expensive, due to manufacturing techniques, to produce a 6% cobalt cermet in the thickness needed for this type of application. They are also more difficult to attach to the pipes than the ceramics. It is easier and cheaper to grind alumina to the dimensional tolerances needed than to grind a cermet to a similar tolerance Although in the long run a cermet might be the best choice, due to fewer downtimes and repairs that might be needed, the initial capitalization costs might be to great.

CHAPTER 7

CONCLUSIONS

1) From the fifteen materials tested for erosion resistance three different mechanisms were observed:

   i) Glass showed a typical brittle response to particle impact with cracks initiating from beneath a central region of crushed material.

   ii) The Co-WC cermets had a more ductile than brittle response to particle impact with the greatest material loss occurring at 60° impact.

   iii) The aluminas were eroded via crack initiation and propagation from beneath a region of elastic/plastic deformation.

2) The conditions used for the erosion testing revealed two threshold effects below which the erosion rate is considerably reduced. A particle velocity threshold was found between 30m/s and 40m/s and an impact angle threshold between 45° and 60°.

3) A direct correlation between erosion rate and fracture toughness was found. Modulus of rupture also showed a good correlation while target hardness showed no correlation to erosion rate.

4) An increase in erodent hardness caused an increase in the erosion rate for all materials. There is a sharp increase in the erosion rate as the relative hardness ratio between target and eodent approaches unity.

5) Fine grained aluminas had a greater erosion resistance than a similar material with a larger grain size.

7) Of all the materials tested the 6%Co-WC cermet showed the greatest erosion resistance at all angles of impact. Depending on initial capitalization costs it is the best choice of lining material.

REFERENCES

1. G.P Tilly "Erosion caused by impact of solid particles" Treatise on Materials Science & Technology vol 13 1979 p287-319.

2. E Raask "Impact erosion wear caused by pulverised coal and ash" Proceedings 5th International Conference on Erosion by Solid and Liquid Impact.

3. C.M Preece "Erosion of Metals and Alloys" Nato Advanced Study Institute proceeding of 1975 conference on Surface Effects in Crystal Plasticity 1976 p889-909.

4. I Finnie "Erosion of surfaces by solid particles" Wear vol 3 1960 p87-103.

5. G.P Tilly "Two stage mechanism of ductile erosion" Wear 23 1973 p87-96.

6. A.V Levy "The platelet mechanism of erosion of ductile metals" Wear vol 108 1986 p1-21.

7. B.R Lawn, A.G Evans & D.B Marshall "Elastic/Plastic Indentation Damage in Ceramics: The Median/Radial Crack System" Journal of American Ceramic Society 1980 p574-581.

8. B.R Lawn & D.B Marshall "Indentation fracture & strength degradation in ceramics" Fracture Mechanics of Ceramics P.C Bradt and F.F Lange (eds) Plenum Press New York p205-229.

9. A.G Evans, M.E Gulden & M Rosenblatt "Impact damage in brittle materials in the elastic-plastic response regime "Proceedings of the Royal Society, London A361 1978 p343-365.

10. B Lawn & R Wilshaw "Indentation fracture: Principles and applications "Journal of Materials Science vol 10 1975 p1049-1081.

11. C.M Perrott "Elastic-Plastic Indentation: Hardness & Fracture" Wear 45 1977 p293-309.

12. Wada as quoted by S Srinivasan and R.O Scattergood "Effect of erodent hardness on erosion of brittle materials" Wear vol 128 1988 pp139-152.

13. S Srinivasan & R.O Scattergood "Effect of erodent hardness on erosion of brittle material" Wear 128 1988 p139-152.

14. I.M Hutchings "Transitions, Threshold Effect and Erosion Maps" Erosion of Ceramic Materials 1992 p75-92.

15. S.M Wiederhorn and B.J Hockey "Effect of material parameters on the erosion resistance of brittle materials" Journal of Materials Science and Technology vol 18 1983 p766-780.

16. B.R Lawn & M.V Swain "Microfracture beneath point indentations in brittle solids" Journal of Materials Science vol 10 1975 p113-122.

17. V.D Krstic "Grain size dependence of fracture stress in anisotropic brittle solids" Journal of Materials Science and Technology vol 23 1988 p259-266.

18. C.B Ponton & R.D Rawlings "Vickers indentation fracture toughness test" Materials Science and Technology vol 5 1989 p865-872.

19. K Anand & H Conrad "Microstructure and Scaling Effects in the Damage of WC-Co alloys by Single Impacts of Hard Particles" Journal of Materials Science vol 23 1988 p2931-2942.

20. H.C Lee & J Gurland "Hardness and Deformation of Cemented Tungsten Carbide Materials Science & Engineering 33 1978 p125-133.

21. K Anand and H Conrad "Microstructure effects in the erosion of cemented carbides." Wear of Materials vol 1 1989 p136-142.

22. J.R Zhou & S Bahadur " Effect of blending of Silcon Carbide particles on varying sizes on the erosion of Ti-6Al-4V" Wear 132 1989 p235-246.

23. S Bahadur & R Badruddin "Erodent particle characterization and the effect of particle size and shape on erosion" Wear 138 1990 p189-208.

24. G Sundararajan "The depth of plastic deformation beneath eroded surfaces: the influence of impact angle & velocity, particle shape and material properties" Wear 149 1991 p129-153.

25. G.P Tilly & W Sage "The interaction of particle and material behaviour in erosive processes" Wear 16 1970 p447-465.

26. J.L Routbort & A.P.L Turner "The Erosion Rate of Reaction Bonded SiC Containing Various Amounts of Free Silicon" Wear 84 1983 p381-385.

27. P.G Shewmon "Particle size threshold in the erosion of metals" Wear 68 1981 p253-258.

28. S.M Wiederhorn & B.R Lawn "Strength Degradation of Glass Impacted with Sharp Particles: I, Annealed Surfaces" Journal of the American Ceramic Society vol 62 1979 p66-70.

29. R.A Vaughn & A Ball "Erosion Processes for Hard Materials Subjected to Impact by Different Erodents" Journal of Hard Materials vol 2 1991 p257-269.

30. R.A Vaughn "The Effects of Hardness, Toughness, Microstructure and Thermomechanical Heating on the Erosion of Ceramic and Ultrahard Materials" MSc Thesis 1991.

31. L Murugesh & R.O Scattergood "Effect of erodent properties on the erosion of alumina" Journal of Materials Science vol 26 1991 p5456-5466.

32. K Breder, J.E Ritter & K Jakus "Strength Degradation in Polycrystalline Alumino due to Sharp-Particle Impact Damage" Journal of the American Ceramic Society vol71 1988 p1154-1158.

33. UUemous and Kleis "A critical analysis of erosion problems which have been little studied" Wear vol 31 1975 p403.

34. S.M Wiederhorn, B.R Lawn & B.J Hockey "Effect of Particle Impact Angle on Strength Degradation of Glass" Journal of the American Ceramic Society vol 62 1979 p639-640.

35. S Dosanjh & J.A.C Humphrey "The influence of turbulence on erosion by a particle-laden fluid jet" Wear 102 1985 p309-330.

36. J.A Laitone "Aerodynamic effects in the erosion process" Wear 56 1979 p239-246.

37. W Tabakoff, A Hamed & B Beacher "Investigation of gas particle flow in an erosion wind tunnel" Wear 86 1983 p73-88.

38. E Raask "Pipe curvature and impact angle" Erosion wear in coal utilization Hemisphere Publishing New York 1988 p378-384.

39. G.L Bosch "The Minerology and Chemistry of Pulverised Fuel Produced by three South African Power Stations" MSc UCT 1990.

40. C.S Hurlbut "Dana's Manual of Mineralogy" J Willy & Sons London 1959 p494.

41. M.J Murray 1977 "Fracture of WC-Co Alloys: An example of spatially constrained crack tip opening displacement" Proceedings of the Royal Society, London A356 p483-508.

42. T.M Karlson "The erosive characteristics of South African pulverized fuels" MSc Thesis UCT 1985.

43. K Niihara, R Morena, and D Hasselman "Evaluation of K_{IC} of brittle solids by the indentation method with low crack-to-indent ratios" Journal of Materials Science Letters vol 1 1982 p13-16.

44. A.G Evans & E.A Charles "Fracture toughness determination by indentation" Journal of American Ceramic Society 1979 p371-372.

45. P.H Shipway & I.M Hutchings "The Influence of Particle Properties on the Erosive Wear of Sintered Boron Carbide" Wear of Materials ASME 1991 p63-70.

46. B.R Lawn & D.B Marshall "Hardness, Toughnes< and Brittleness: An Indentation Analysis" Journal of American Ceramic Society vol 62 p347-351.

47. D.B Marshall, B.R Lawn & A.G Evens "Elastic/Plastic Indentation Damage in Ceramics: The Lateral Crack System" Journal of American Ceramic Society vol 65 p561-566.

48. D.J Clinton "A Guide to Polishing & Etching of Technical & Engineering Ceramics" Institute of Ceramics Stoke-on-Trent 1987.

49. S.M Wiederhorn, D.B Marshall & B.R Lawn " Strength Degradation of Glass Impacted with Sharp Particles: II Tempered Surfaces" Journal of the American Ceramic Society vol 62 1979 p71-74.

50. R.C Pennefather "The solid Particle erosion of WC-Co Alloys" MSc UCT 1986.

51. H Conrad, Y Shin & G.A Sargent " Erosion of Sintered WC-Co Alloys" Proceedings of the Internatiuonal Conference on Recent Developements in Special Steels and Hard Metals, CSIR Pretoria South Africa 1982 p423-429.

52. G.L Sheldon & I Finnie "On the Ductile Behaviour of Nominally Brittle Materials During Erosive Cutting" Journal of Engineering for Industry Transactions of the ASME 1966 p387-392.

53. R.F Cook & G.M Pharr "Direct Observatio & Analysis of Indentation Cracking in Glass & Ceramics" Journal of the American Ceramic Society vol 73 1990 p787.

54. J.E Ritter "Strength Degradation of Ceramics due to Solid Particle Erosion" Erosion of Ceramic Materials 1992 p93-106.

55. A.J Sparks & I.M Hutchings "Transitions in the erosive wear behaviour of a glass-ceramic" Wear of Materials ASME 1991 vol 1 p367-374.

56. J.L Routbort & R.O Scattergood "Solid-particle erosion of ceramic composites" Erosion of Ceramic Materials 1992 p23-50.

57. K Anand, C Morrison, R,O Scattergood, H Conrad, J.L Routbort & R Warren: 2nd International Conference Science of Hard Materials 1986, Rhodes, Adam Hilger Ltd, 949.

58. B Mussler M.V Swain & N Claussen "Dependece of Fracture Toughness of Alumina on Grain Size and Test Technique" Journal of American Ceramic Society vol 65 p566-571.

59. R.A Vaughan & A Ball "The Effect of Hardness and Toughness on the Erosion of Ceramic And Ultrahard Materials" Wear of Materials 1991 p71-75.

60. A.W Ruff & L.K Ives "Measurement of solid particle velocity in erosive wear" Wear vol 35 1975 p195-199.

APPENDIX 1

The following two tables, A1.1 and A1.2, are of the erosion results of the materials tested, and include both the corrected and uncorrected results.

NAME	EROSION 90 DEG cm^3/g (*10^-5)	EROSION 60 DEG cm^3/g (*10^-5)	EROSION 45 DEG cm^3/g (*10^-5)	EROSION 30 DEG cm^3/g (*10^-5)	Corrected EROSION 90 DEG cm^3/g (*10^-5)	Corrected EROSION 60 DEG cm^3/g (*10^-5)	Corrected EROSION 45 DEG cm^3/g (*10^-5)	Corrected EROSION 30 DEG cm^3/g (*10^-5)
BASALT	25.979	12.517	5.350	2.420	49.243	23.613	11.020	7.597
MD	28.080	13.807	4.846	1.808	53.226	26.047	9.983	5.676
MZF	0.903	0.730	0.373	0.173	1.712	1.377	0.769	0.545
M97F	0.855	0.816	0.329	0.170	1.621	1.539	0.677	0.535
M97	1.369	1.230	0.397	0.178	2.595	2.320	0.818	0.558
M94	1.239	1.043	0.468	0.177	2.349	1.968	0.964	0.556
M94F	0.759	0.575	0.296	0.123	1.439	1.085	0.609	0.386
M99	0.750	0.697	0.300	0.165	1.422	1.315	0.618	0.519
90%Al	0.527	0.479	0.248	0.100	0.999	0.904	0.511	0.314
GLASS	65.200	28.900	14.600	5.000	123.587	54.520	30.076	15.700
MT	1.500	1.300	0.460	0.213	2.843	2.452	0.948	0.669
87%US	1.060	0.970	0.336	0.168	2.009	1.830	0.692	0.528
6%WC	0.083	0.118	0.067	0.028	0.158	0.223	0.137	0.087
10%WC	0.217	0.252	0.135	0.048	0.411	0.475	0.278	0.150
90%Germ	2.051	1.752	0.868	0.447	3.888	3.305	1.788	1.404

Table A1.1: Table of the erosion rates of the different materials at the four different angles of impact.

Conditions 60 DEG	EROSION M94 cm^3/g (*10^-5)	EROSION M94F cm^3/g (*10^-5)	Corrected EROSION M94 cm^3/g (*10^-5)	Corrected EROSION M94F cm^3/g (*10^-5)
40m/s				
120 grit silica	1.043	0.575	1.968	1.085
120 grit alumina	1.707	1.351	3.210	2.540
120 grit SiC	4.490	3.094	8.461	5.836
120 grit silica				
30m/s	0.557	0.352	1.051	0.664
50m/s	1.149	0.697	2.098	1.315
40m/s				
140 grit silica	1.141	0.661	2.163	1.249
< 100 grit silica	0.589	0.430	1.111	0.810

Table A1.2: Table of the erosion rates of M94 and M94F for the different conditions and erodents.

APPENDIX 2

The velocities of the different erodents were all calculated using the Ruff and Ives (60) method outlined in appendix 3. The results obtained for the three different SiO_2 sizes are illustrated on the graph below figure A2.

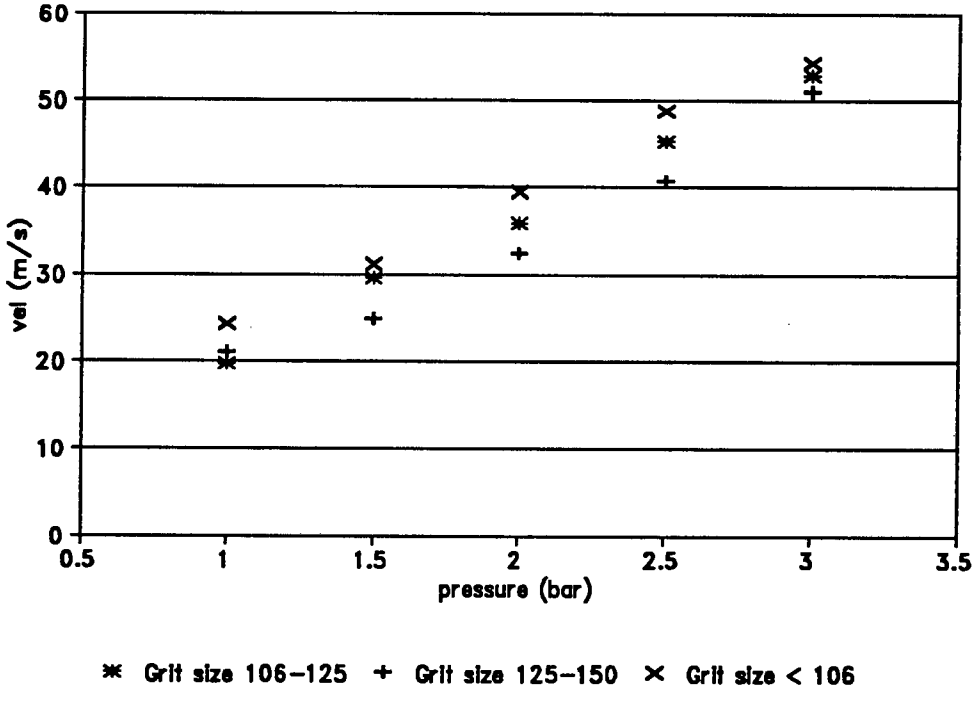

Fig A2: Graph of pressure vs velocity of the different SiO_2 grit sizes.

Similar graphs were obtained for the other erodents that were used during the project.

APPENDIX 3

The particle velocities were all measured using the Ruff and Ives (60) method of two parallel rotating discs illustrated below in figure A3. A slit is placed in the first disc such that when the two discs are placed in the path of an air/particle stream some of the particles will strike the back disc and leaving a mark. If these discs are then rotated at a constant rate the particles passing through the slit in the front disc will strike the back disc at a point away from the first mark. The distance between the two marks can then be measured and related to the particle velocity via the following equation:

$$V = 2rwL\emptyset/S$$

Where: r = radius from disc centre
w = disc rotational velocity
L = disc seperation
Ø = Pi
S = linear seperation of the two marks

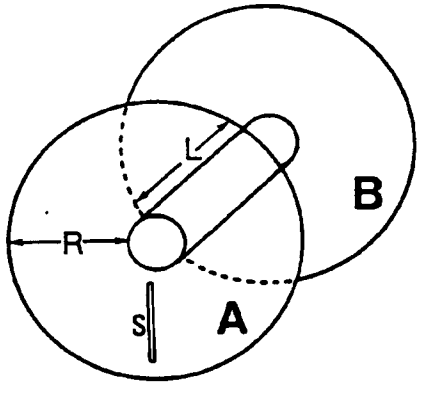

Fig A3: Schematic diagram of the two parallel disks.

APPENDIX 4

In order to determine the reproducibility of the tests, two erosion tests were carried out at 60° and 40 m/s using 120 grit SiO_2. The two materials chosen were M94 and 90%JAP the results, found on graphs A4.1 and A4.2, show that a high degree of reproducibility can be expected from these materials.

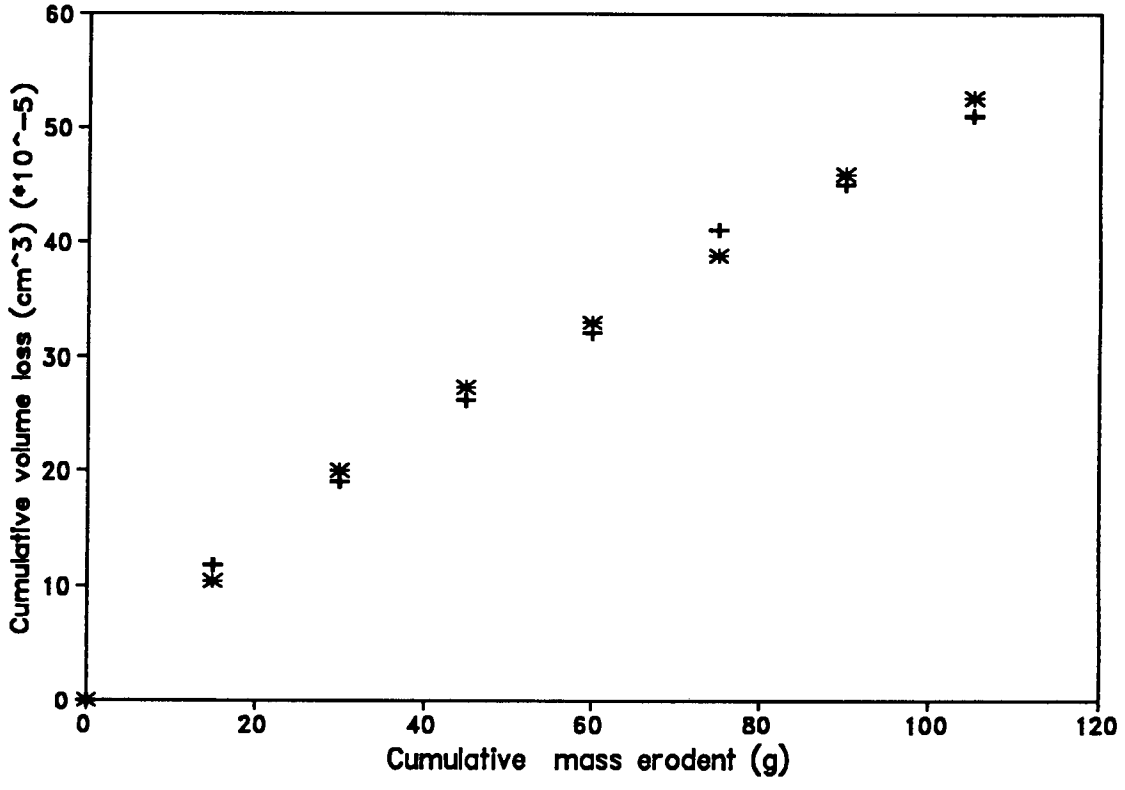

Fig A4.1: The reproducibility of the 90%Jap sample eroded at 60° and 40 m/s using 120 grit SiO2.

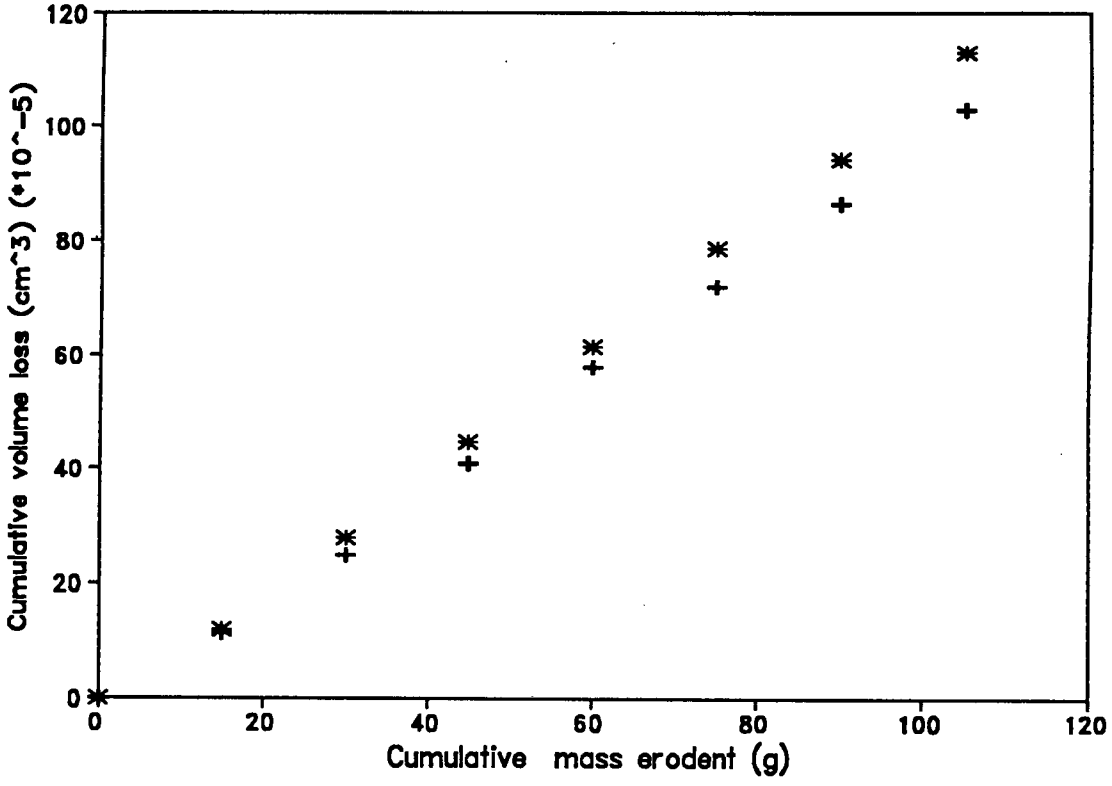

Fig A4.1: The reproducibility of the M94 sample eroded at 60° and 40 m/s using 120 grit SiO_2.